

## HIGH-RESOLUTION TIMING OBSERVATIONS OF SPIN-POWERED PULSARS WITH THE *AGILE* GAMMA-RAY TELESCOPE\*

A. PELLIZZONI<sup>1</sup>, M. PILIA<sup>1,2</sup>, A. POSSENTI<sup>2</sup>, F. FORNARI<sup>1</sup>, P. CARAVEO<sup>1</sup>, E. DEL MONTE<sup>3</sup>, S. MEREGHETTI<sup>1</sup>, M. TAVANI<sup>3,4</sup>, A. ARGAN<sup>3</sup>, A. TROIS<sup>3</sup>, M. BURGAY<sup>2</sup>, A. CHEN<sup>1,5</sup>, I. COGNARD<sup>6</sup>, E. COSTA<sup>3</sup>, N. D’AMICO<sup>2,7</sup>, P. ESPOSITO<sup>1,8,9</sup>, Y. EVANGELISTA<sup>3</sup>, M. FEROCI<sup>3</sup>, F. FUSCHINO<sup>10</sup>, A. GIULIANI<sup>1</sup>, J. HALPERN<sup>11</sup>, G. HOBBS<sup>12</sup>, A. HOTAN<sup>13</sup>, S. JOHNSTON<sup>12</sup>, M. KRAMER<sup>14</sup>, F. LONGO<sup>15</sup>, R. N. MANCHESTER<sup>12</sup>, M. MARISALDI<sup>10</sup>, J. PALFREYMAN<sup>16</sup>, P. WELTEVREDE<sup>12</sup>, G. BARBIELLINI<sup>15</sup>, F. BOFFELLI<sup>8,9</sup>, A. BULGARELLI<sup>10</sup>, P. W. CATTANEO<sup>8</sup>, V. COCCO<sup>3</sup>, F. D’AMMANDO<sup>3,4</sup>, G. DE PARIS<sup>3</sup>, G. DI COCCO<sup>3</sup>, I. DONNARUMMA<sup>3</sup>, M. FIORINI<sup>1</sup>, T. FROYSLAND<sup>4,5</sup>, M. GALLI<sup>17</sup>, F. GIANOTTI<sup>10</sup>, A. HARDING<sup>18</sup>, C. LABANTI<sup>10</sup>, I. LAPSHOV<sup>3</sup>, F. LAZZAROTTO<sup>3</sup>, P. LIPARI<sup>19</sup>, F. MAURI<sup>8</sup>, A. MORSELLI<sup>20</sup>, L. PACCIANI<sup>3</sup>, F. PEROTTI<sup>1</sup>, P. PICOZZA<sup>20</sup>, M. PRESTI<sup>21</sup>, G. PUCELLA<sup>3</sup>, M. RAPISARDA<sup>22</sup>, A. RAPPOLDI<sup>8</sup>, P. SOFFITTA<sup>3</sup>, M. TRIFOGLIO<sup>10</sup>, E. VALLAZZA<sup>15</sup>, S. VERCELLONE<sup>1</sup>, V. VITTORINI<sup>4</sup>, A. ZAMBRA<sup>1</sup>, D. ZANELLO<sup>19</sup>, C. PITTORI<sup>23</sup>, F. VERRECCHIA<sup>23</sup>, B. PREGER<sup>23</sup>, P. SANTOLAMAZZA<sup>23</sup>, P. GIOMMI<sup>23</sup>, AND L. SALOTTI<sup>24</sup>

<sup>1</sup> INAF/IASF–Milano, via E. Bassini 15, I-20133 Milano, Italy; [alberto@iasf-milano.inaf.it](mailto:alberto@iasf-milano.inaf.it)

<sup>2</sup> INAF–Osservatorio Astronomico di Cagliari, loc. Poggio dei Pini, strada 54, I-09012 Capoterra, Italy

<sup>3</sup> INAF/IASF–Roma, via del Fosso del Cavaliere 100, I-00133 Roma, Italy

<sup>4</sup> Dipartimento di Fisica, Università “Tor Vergata,” via della Ricerca Scientifica 1, I-00133 Roma, Italy

<sup>5</sup> CIFS–Torino, viale Settimio Severo 3, I-10133, Torino, Italy

<sup>6</sup> Laboratoire de Physique et Chimie de l’Environnement, CNRS, F-45071 Orleans, France

<sup>7</sup> Dipartimento di Fisica Università di Cagliari, Cittadella Universitaria, I-09042 Monserrato, Italy

<sup>8</sup> INFN–Pavia, via Bassi 6, I-27100 Pavia, Italy

<sup>9</sup> Dipartimento di Fisica Nucleare e Teorica, Università di Pavia, via A. Bassi 6, Pavia, I-27100, Italy

<sup>10</sup> INAF/IASF–Bologna, via Gobetti 101, I-40129 Bologna, Italy

<sup>11</sup> Columbia Astrophysics Laboratory, Columbia University, New York, NY 10027, USA

<sup>12</sup> Australia Telescope National Facility, CSIRO, P.O. Box 76, Epping NSW 1710, Australia

<sup>13</sup> Curtin University of Technology, 78 Murray Street, Perth, WA 6000, Australia

<sup>14</sup> University of Manchester, Jodrell Bank Observatory, Macclesfield, Cheshire SK11 9DL, UK

<sup>15</sup> Dipartimento di Fisica Università di Trieste and INFN–Trieste, via Valerio 2, I-34127 Trieste, Italy

<sup>16</sup> School of Mathematics and Physics, University of Tasmania, Hobart, TAS 7001, Australia

<sup>17</sup> ENEA–Bologna, via Biancamano 2521, I-40059 Medicina (BO), Italy

<sup>18</sup> Astrophysics Science Division, NASA/Goddard Space Flight Center, Greenbelt, MD 20771, USA

<sup>19</sup> INFN–Roma “La Sapienza,” piazzale A. Moro 2, I-00185 Roma, Italy

<sup>20</sup> INFN–Roma “Tor Vergata,” via della Ricerca Scientifica 1, I-00133 Roma, Italy

<sup>21</sup> Dipartimento di Fisica, Università dell’Insubria, via Valleggio 11, I-22100 Como, Italy

<sup>22</sup> ENEA–Roma, via E. Fermi 45, I-00044 Frascati (Roma), Italy

<sup>23</sup> ASI–ASDC, via G. Galilei, I-00044 Frascati (Roma), Italy

<sup>24</sup> ASI, viale Liegi 26, I-00198 Roma, Italy

Received 2008 July 4; accepted 2008 October 5; published 2009 February 5

### ABSTRACT

*Astro-rivelatore Gamma ad Immagini LEggero (AGILE)* is a small gamma-ray astronomy satellite mission of the Italian Space Agency dedicated to high-energy astrophysics launched in 2007 April. Its  $\sim 1 \mu\text{s}$  absolute time tagging capability coupled with a good sensitivity in the 30 MeV–30 GeV range, with simultaneous X-ray monitoring in the 18–60 keV band, makes it perfectly suited for the study of gamma-ray pulsars following up on the *Compton Gamma Ray Observatory*/EGRET heritage. In this paper, we present the first *AGILE* timing results on the known gamma-ray pulsars Vela, Crab, Geminga, and B1706–44. The data were collected from 2007 July to 2008 April, exploiting the mission Science Verification Phase, the Instrument Timing Calibration, and the early Observing Pointing Program. Thanks to its large field of view, *AGILE* collected a large number of gamma-ray photons from these pulsars ( $\sim 10,000$  pulsed counts for Vela) in only few months of observations. The coupling of *AGILE* timing capabilities, simultaneous radio/X-ray monitoring, and new tools aimed at precise photon phasing, also exploiting timing noise correction, unveiled new interesting features at the submillisecond level in the pulsars’ high-energy light curves.

**Key words:** gamma rays: observations – pulsars: general – pulsars: individual (Vela, Crab, Geminga, PSR B 1706–44) – stars: neutron

*Online-only material:* color figure

### 1. INTRODUCTION

Among the  $\sim 1800$  known rotation-powered pulsars, mainly observed in the radio band, seven objects have been identified as gamma-ray emitters, namely Vela (B0833–45),

Crab (B0531+21), and Geminga (J0633+1746), B1706–44, B1509–58, B1055–52, and B1951+32 (Thompson 2004). In addition, B1046–58 (Kaspi et al. 2000), B0656+14 (Ramana-murthy et al. 1996), and J0218+4232 (Kuiper et al. 2000, 2002) were reported with lower confidence (probability of the periodic signal occurring by chance in gamma rays of  $\sim 10^{-4}$ ). In spite of the paucity of pulsar identifications, gamma-ray observations are a valuable tool for studying particle acceleration sites and

\* Based on observations obtained with *AGILE*, an ASI (Italian Space Agency) science mission with instruments and contributions directly funded by ASI.

emission mechanisms in the magnetospheres of spin-powered pulsars.

So far, spin-powered pulsars were the only class of Galactic sources firmly identified by *Compton Gamma Ray Observatory* (CGRO)/EGRET and presumably some of the unidentified gamma-ray sources will turn out to be associated with young and energetic radio pulsars discovered in recent radio surveys (Manchester et al. 2001; Kramer et al. 2003). In fact, several unidentified gamma-ray sources have characteristics similar to those of the known gamma-ray pulsars (hard spectrum with high-energy cutoff, no variability, possible X-ray counterparts with a thermal/nonthermal component, and no prominent optical counterpart), but they lack a radio counterpart as well as a supernova remnant and/or pulsar wind nebula association. Radio-quiet, Geminga-like objects have been invoked by several authors (Romani & Yadigaroglu 1995; Yadigaroglu & Romani 1995; Harding et al. 2007) but without evidence of pulsation in gamma rays, no identification has been confirmed.

Apart from the Crab and B1509–58, whose luminosities peak in the 100 keV and about 30 MeV range respectively, the energy flux of the remaining gamma-ray pulsars is dominated by the emission above 10 MeV with a spectral break in the GeV range.

*Astro-rivelatore Gamma ad Immagini LEggero* (AGILE) is a small scientific mission of the Italian Space Agency dedicated to high-energy astrophysics (Tavani et al. 2006, 2009) launched on 2007 April 23. Its sensitivity in the 30 MeV–30 GeV range, with simultaneous X-ray imaging in the 18–60 keV band, makes it perfectly suited for the study of gamma-ray pulsars. Despite its small dimensions and weight ( $\sim 100$  kg), the new silicon detector technology employed for the AGILE instruments yields overall performances as good as, or better than, those of previous bigger instruments. High-energy photons are converted into  $e^+/e^-$  pairs in the Gamma-Ray Imaging Detector (GRID; a Silicon–Tungsten tracker; Prest et al. 2003; Barbiellini et al. 2001), allowing for an efficient photon collection with an effective area of  $\sim 500$  cm<sup>2</sup>, and for an accurate arrival direction reconstruction ( $\sim 0.5$  at 1 GeV) over a very large field of view (FOV), covering about 1/5 of the sky in a single pointing. The Cesium–Iodide minicalorimeter (Labanti et al. 2006) is used in conjunction with the tracker for photon energy reconstruction while supporting the anticoincidence shield in the particle background rejection task (Perotti et al. 2006). The AGILE/GRID is characterized by the smallest dead time ever obtained for gamma-ray detection (typically 200  $\mu$ s) and time tagging with uncertainty near  $\sim 1$   $\mu$ s. The SuperAGILE hard X-ray monitor is positioned on top of the GRID. SuperAGILE is a coded aperture instrument operating in the 18–60 keV energy band with about 15 mCrab sensitivity in 1 day integration, 6 arcmin angular resolution, and  $\sim 1$  sr FOV (Feroci et al. 2007; Costa et al. 2001).

In this work, we analyze all available AGILE/GRID data suitable for timing analysis collected up to 2008 April 10 for the four known gamma-ray pulsars included in the AGILE Team source list<sup>25</sup>: Vela, Crab, Geminga, and B1706–44. The other two EGRET pulsars, B1055–52 and B1951+32, are part of the AGILE Guest Observer program. As expected, only the Crab pulsar has been detected by SuperAGILE and the X-ray data have been used to crosscheck and test AGILE timing performances.

The AGILE observations, as well as the criteria for photon selections, are presented in Section 2. The observations and the timing analysis from the parallel radio and X-ray observations of the four targets are described in Section 3. The procedures for the timing analysis of gamma-ray data are introduced in Section 4 and the results of their application are reported in Section 5, where timing calibration tests are also dealt with. Discussion of the scientific results and conclusions are the subjects of Sections 6 and 7, respectively.

## 2. AGILE OBSERVATIONS AND DATA REDUCTION

The AGILE spacecraft was placed in a Low Earth Orbit (LEO) at  $\sim 535$  km mean altitude with an inclination of  $\sim 2.5^\circ$ . Therefore, Earth occultation strongly affects exposure along the orbital plane, as well as a high particle background rate during South Atlantic Anomaly (SAA) transits. However, the exposure efficiency is  $> 50\%$  for most AGILE revolutions. AGILE pointings consist of long exposures (typically lasting 10–30 days) slightly drifting ( $\lesssim 1^\circ$ /day) with respect to the starting pointing direction in order to match solar-panels' illumination constraints. The relatively uniform values of the effective area and point-spread function (PSF) within  $\sim 40^\circ$  from the center of the FOV of the GRID allow for one-month pointings without significant vignetting in the exposure of the target region.

Pulsar data were collected during the mission Science Verification Phase (SVP; 2007 July–November) and early pointings<sup>26</sup> (2007 December–2008 April) of the AO 1 Observing Program. It is worth noting that a single AGILE pointing on the Galactic Plane embraces about one-third of it, allowing for simultaneous multiple source targeting (e.g., the Vela and Anti-Center regions in the same FOV with Crab, Geminga, and Vela being observed at once; Figure 1).

The AGILE Commissioning and SVP lasted about seven months from 2007 April 23 to November 30, also including Instrument Time Calibration. On 2007 December 1, baseline nominal observations and a pointing plan started together with the Guest Observer program AO 1. Timing observations suitable for pulsed signal analysis of the Vela pulsar started in mid 2007 July (at orbit 1146) after engineering tests on the payload.

The Vela region was observed (with optimal exposure efficiency) for  $\sim 40$  days during the SVP and again for  $\sim 30$  days in AO 1 pointing number 3 (2008 January 8–February 1). PSR B1706–44 was within the Vela and Galactic Center pointings for  $\sim 30$  days during the SVP and for  $\sim 45$  days during AO 1 pointing numbers 5 and 6 (2008 February 14–March 30). The Anti-Center region (including Crab and Geminga) was observed for  $\sim 40$  days, mostly in 2007 September and in 2008 April (AO 1 pointing number 7) with the addition of other sparse short Crab pointings for SuperAGILE calibration purposes during the SVP (see Table 1 and Figure 2 for details about targets' coverage).

GRID data of the relevant observing periods were grouped in 20 subsets of 200 orbits each (corresponding to  $\sim 15$  days of observation) starting from orbit 1146 (54,294 MJD). Data screening, particle background filtering and event direction and

<sup>25</sup> See <http://agile.asdc.asi.it> for details about AGILE data policy and target list.

<sup>26</sup> 1. Cygnus Field 1 ( $l = 89^\circ$ ,  $b = 9^\circ$ ), 2. Virgo Field ( $l = 264^\circ$ ,  $b = 56.5^\circ$ ), 3. Vela Field ( $l = 283^\circ$ ,  $b = -6.8^\circ$ ), 4. South Gal. Pole ( $l = 240^\circ$ ,  $b = -50^\circ$ ), 5. Musca Field ( $l = 303^\circ$ ,  $b = -9^\circ$ ), 6. Gal. Center ( $l = 332^\circ$ ,  $b = 0^\circ$ ), 7. Anti-Center ( $l = 193^\circ$ ,  $b = 8.1^\circ$ ).

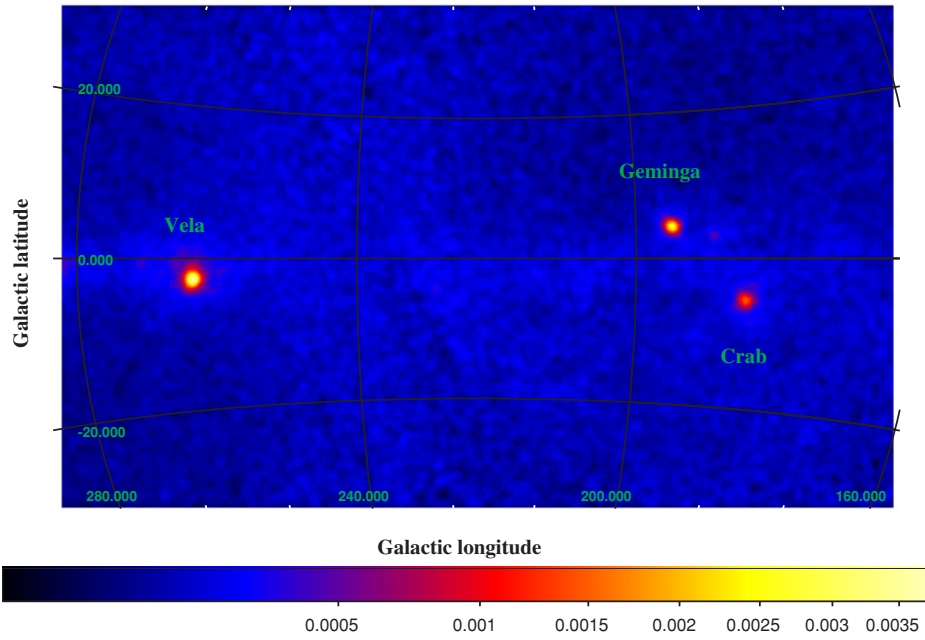


**Figure 1.** Gaussian-smoothed *AGILE* intensity map ( $\sim 120^\circ \times 60^\circ$ , units:  $\text{ph cm}^{-2} \text{s}^{-1} \text{sr}^{-1}$ ,  $E > 100 \text{ MeV}$ ) in Galactic coordinates integrated over the whole observing period (2007 July 13–2008 April 10) and centered at  $l = 223^\circ$  and  $b = 0^\circ$ . The *AGILE* FOV (radius  $\sim 60^\circ$ ) can embrace in a single pointing Vela ( $l = 263^\circ 6$ ,  $b = -2^\circ 8$ ), Geminga ( $l = 195^\circ 1$ ,  $b = 4^\circ 3$ ), and Crab ( $l = 184^\circ 6$ ,  $b = -5^\circ 8$ ) as well as diffuse emission from the Galactic Disk.

(A color version of this figure is available in the online journal.)

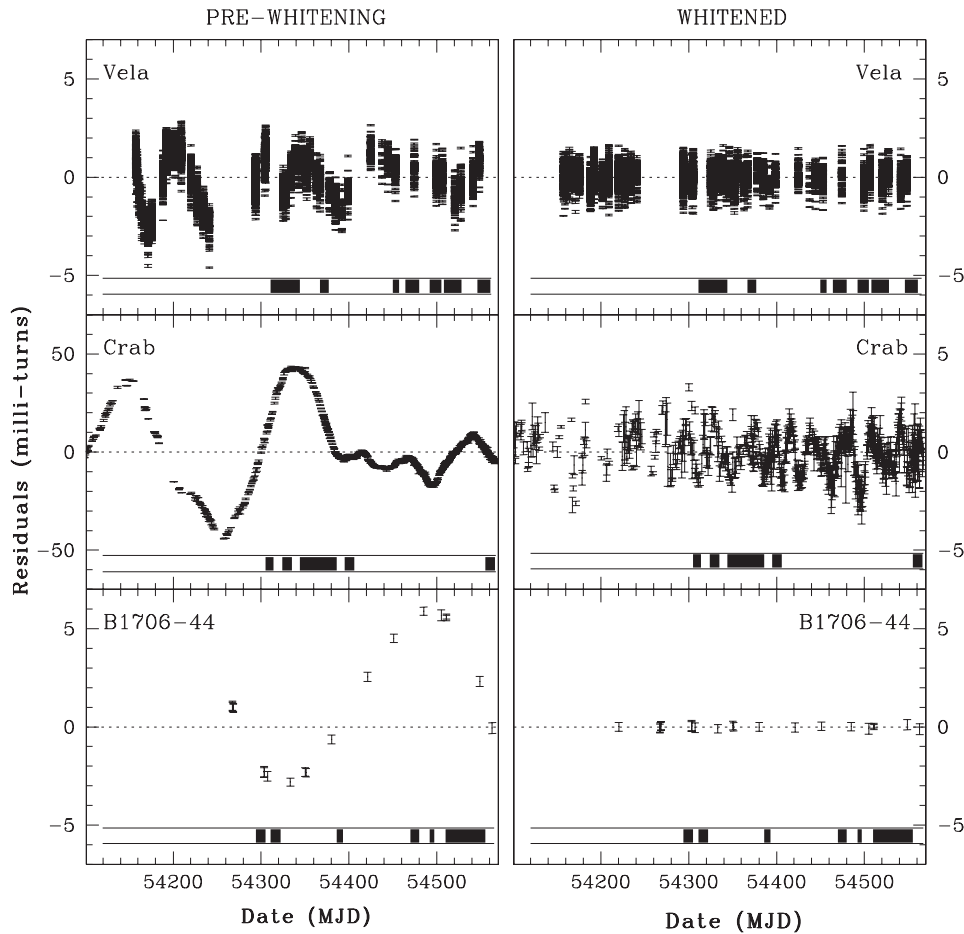


**Figure 2.** Postfit timing residuals (in milliturns) as a function of the Modified Julian Day resulting from the observation at 1.4 GHz of the three radio pulsars, which are discussed in this paper: from the top Vela, Crab, and PSR B1706–44. The panels in the left (right) column report the residuals of the best available timing solutions obtained over the data span not including (including) the correction of the timing noise via the use of the  $\Delta R$  term (see Section 4). Note that for the Crab pulsar, the scale on the vertical axis of the panel in the right column is amplified by a factor of 10 with respect to that in the left panel. The time intervals corresponding to the useful *AGILE* pointings for each target are also given as the black sections of the bar at the bottom of each panel.

**Table 1**  
Observation Parameters of the Relevant Data Subsets (Grouped in Uninterrupted Target Observations)

PSR	ObsID <sup>a</sup>	$T_{\text{FIRST}}$ (MJD)	$T_{\text{LAST}}$ (MJD)	$\langle\theta\rangle^b$ (deg)	Total Counts <sup>c</sup>	Exposure <sup>d</sup> ( $10^8 \text{ cm}^2 \text{ s}$ )
Vela	SVP 1	54294.552	54305.510	26.2	6440	1.87
Vela	SVP 2-3-4	54311.512	54344.569	40.9	12651	3.26
Vela	SVP 5	54358.525	54359.521	41.4	391	0.11
Vela	SVP 6	54367.525	54377.521	48.9	1355	0.26
Vela	SVP 8	54395.554	54406.501	55.3	113	0.03
Vela	AO 1 2	54450.540	54457.157	56.2	564	0.01
Vela	AO 1 2-3	54464.784	54480.966	22.1	4726	3.13
Vela	AO 1 3-4	54492.948	54505.377	43.2	6293	1.16
Vela	AO 1 4-5-6	54508.528	54528.537	43.6	9747	2.22
Vela	AO 1 6	54546.095	54561.427	41.7	703	0.17
Vela	Total <sup>e</sup>	54294.552	54561.427	36.1	42983	12.22
Vela	Gamma <sup>f</sup>	54294.552	54561.427	36.1	6140	5.28
Geminga	SVP 2	54308.871	54314.507	55.0	187	0.06
Geminga	SVP 3	54324.514	54335.508	41.3	781	0.24
Geminga	SVP 4-5-6-7	54344.518	54351.235	22.2	17823	6.19
Geminga	SVP 8	54395.520	54406.504	37.6	1926	0.48
Geminga	AO 1 6	54528.531	54529.270	50.7	38	0.01
Geminga	AO 1 6	54546.093	54549.428	39.0	132	0.03
Geminga	AO 1 6-7	54555.514	54566.5	11.7	4860	2.03
Geminga	Total <sup>e</sup>	54308.871	54566.5	20.2	25962	9.04
Geminga	Gamma <sup>f</sup>	54308.871	54566.5	20.2	3874	4.54
Crab	SVP 1-2	54305.509	54314.50	50.2	2404	0.58
Crab	SVP 3	54324.512	54335.508	28.2	761	0.32
Crab	SVP 4-5-6-7	54344.518	54386.502	23.9	20499	6.41
Crab	SVP 8	54395.518	54406.506	45.4	1537	0.32
Crab	AO 1 3-4	54494.447	54505.390	55.8	350	0.05
Crab	AO 1 4	54508.506	54510.474	54.7	359	0.06
Crab	AO 1 6	54528.531	54529.140	46.9	100	0.02
Crab	AO 1 6	54546.091	54549.423	41.5	176	0.03
Crab	AO 1 6-7	54555.516	54566.5	21.8	4973	1.89
Crab	Total <sup>e</sup>	54305.509	54566.5	26.1	31159	9.68
Crab	Gamma <sup>f</sup>	54305.509	54566.5	26.1	4062	4.11
B1706-44	SVP 1	54294.552	54305.503	50.9	4641	0.91
B1706-44	SVP 2-3-4	54311.531	54322.891	34.5	15657	4.39
B1706-44	SVP 7-8	54386.524	54393.752	41.5	5521	1.28
B1706-44	AO 1 2-3	54470.292	54480.965	53.7	2169	1.46
B1706-44	AO 1 3	54492.948	54497.509	44.9	1507	0.20
B1706-44	AO 1 5-6	54510.482	54555.509	22.4	24219	7.36
B1706-44	Total <sup>e</sup>	54294.552	54555.509	28.7	53714	15.6
B1706-44	Gamma <sup>f</sup>	54294.552	54555.509	28.7	8463	6.56

**Notes.**

<sup>a</sup> Observation ID: SVP=Science Verification Phase (grouped in a subset of 200 orbits, each starting from 1146), AO 1=Scientific Observations Program pointings (see *AGILE* Mission Announcement of Opportunity Cycle-1: <http://agile.asdc.asi.it/>).

<sup>b</sup> Mean off-axis angle.

<sup>c</sup> Source photons + diffuse emission photons + particle background.

<sup>d</sup> Good observing time after dead-time and occultation corrections.

<sup>e</sup> Total G+L class events with  $E > 100 \text{ MeV}$ ,  $5^\circ$  max from pulsar position,  $60^\circ$  max from the FOV center.

<sup>f</sup> High-confidence photon events (G class only) with  $E > 100 \text{ MeV}$ ,  $5^\circ$  max from pulsar position, and  $60^\circ$  max from the FOV center.

energy reconstruction were performed by the *AGILE* Standard Analysis Pipeline (BUILD-15) for each subset with an exposure of  $> 10^6 \text{ cm}^2 \text{ s}$  at  $E > 100 \text{ MeV}$ . Observations affected by coarse pointing, non-nominal settings or intense particle background (e.g., orbital passages in SAA), and albedo events from the Earth's limb were excluded from the processing.

A specific optimization on the events' extraction parameters is performed for each target in order to maximize the signal-to-noise ratio (S/N) for a pulsed signal. The optimal event extraction radius around pulsar positions varies as a function of photon energy (and then it is related to pulsar

spectra) according to the PSF. However, for  $E > 100 \text{ MeV}$  broadband analysis, a fixed extraction radius of  $\sim 5^\circ$  (a value slightly higher than the PSF 68% containment radius) produces comparable results with respect to energy-dependent extraction.

Quality flags define different GRID event classes. The G event class includes events identified with good confidence as photons. Such selection criteria correspond to an effective area of  $\sim 250 \text{ cm}^2$  above 100 MeV (for sources within  $30^\circ$  from the center of the FOV). The L event class includes events typically affected by an order of magnitude higher particle contamination than G, but yielding an effective area of  $\sim 500 \text{ cm}^2$  at

**Table 2**  
The Photon Harvest from the *AGILE* Observations of Gamma-Ray Pulsars

PSR	P (ms)	$\dot{E}$ ( $\text{erg s}^{-1}$ )	$d$ (kpc)	Pulsed Counts <sup>a</sup>	$\chi_r^2$ (dof)	Exposure <sup>b</sup> ( $10^8 \text{ cm}^2 \text{ s}$ )	Pulsed Flux <sup>c</sup> $10^{-8} \text{ ph. cm}^{-2} \text{ s}^{-1}$
Vela	89.3	$6.92 \times 10^{36}$	0.29	$9170 \pm 580$	225.51 (9)	12.22	$940 \pm 60$
Geminga	237.1	$3.25 \times 10^{34}$	0.16	$2200 \pm 480$	10.44 (9)	9.04	$300 \pm 70$
Crab	33.	$4.61 \times 10^{38}$	2.00	$2120 \pm 530$	10.71 (9)	9.68	$270 \pm 70$
B1706–44	102.5	$3.41 \times 10^{36}$	1.82	$2370 \pm 720$	9.11 (9)	15.6	$190 \pm 60$

**Notes.** See text for details on data reduction and timing analysis.

<sup>a</sup> Pulsed counts (G+L event class) with  $E > 100 \text{ MeV}$ ,  $5^\circ$  max from pulsar position,  $60^\circ$  max from the FOV center, 10 bins.

<sup>b</sup> Good observing time after dead-time and occultation corrections.

<sup>c</sup> Calculated with the expression  $C_p f / E$ , where  $C_p$ =pulsed counts,  $E$ =exposure,  $f$ =factor accounting for source counts at an angular distance  $> 5^\circ$  from the source position according to the PSF ( $f \sim 1.25$ ).

$E > 100 \text{ MeV}$ , if grouped with the G class. We performed our timing analysis looking for pulsed signals, using both G class events and the combination of G+L events. In general, the S/N of the pulsed signal is maximized using photons collected within  $\sim 40^\circ$  from the center of GRID FOV and selecting the event class G. For very strong sources, such as Vela, or sources located in low background regions, it is also possible to include photons in the  $40\text{--}60^\circ$  off-axis range and belonging to the G+L event class typically improving the count statistics by up to a factor of 3 (obviously also implying a much higher background), without affecting or even improving the detection significance. For each pulsar, Table 1 summarizes the exposure parameters of the relevant data subsets grouped in uninterrupted target observations. For simplicity and comparison, in Tables 1 and 2, we report observation and detection parameters obtained with the same extraction criteria and energy range. For all observations with the targets within  $60^\circ$  from the pointing direction, we list the average angular distance ( $\theta$ ) of the source position from the pointing direction, the sum of all G+L events with  $E > 100 \text{ MeV}$  whose direction is within  $5^\circ$  from the pulsar position and the G-only events (“gamma photons”), selected with the same criteria. The choice to include all G+L events yields a “dirty” data set: for the case of Vela,  $\sim 10\%$  of the total counts are ascribable to the Galactic Plane and  $> 50\%$  are particle backgrounds ( $\sim 10,000$  source counts). The contamination is reduced in the “gamma” entry, characterized by  $\sim 20\%$  diffuse emission and  $\sim 5\%$  particle background ( $\sim 5000$  source counts). The corresponding exposure for each data subset was calculated with the GRID scientific analysis task AG\_ExpmapGen according to the above parameters. Summing up the photon numbers, we see that the overall photon statistics accumulated (accounting for background contamination) is comparable with that collected by EGRET for the same four pulsars.

A maximum likelihood analysis (ALIKE task) on the *AGILE* data from the sky areas containing the four gamma-ray pulsars yielded source positions, fluxes, and spectra in good agreement with those reported both in the EGRET catalogue for the corresponding 3EG sources (Hartman et al. 1999) and in the revised catalogue by Casandjian & Grenier (2008). As an example, Figure 1 reports an *AGILE* intensity map displaying Vela, Geminga, and Crab. Details on gamma-ray imaging and spectra of the four sources will be reported in future papers when count statistics significantly higher than those currently available are collected and in-flight Calibration files are finalized.

In this paper, we focus on timing analysis. However, it is worth noticing that pulsed counts provide a gamma-ray pulsar flux estimate independent of the likelihood analysis, as described in Section 5.

### 3. RADIO/X-RAY OBSERVATIONS AND TIMING

In order to perform *AGILE* timing calibration through accurate folding and phasing, as described in Sections 4 and 5, respectively, pulsar timing solutions valid for the epoch of *AGILE* observations were required. Thus, a dedicated pulsar monitoring campaign (that will continue during the whole *AGILE* mission) was undertaken, using two telescopes (namely Jodrell Bank and Nançay) of the European Pulsar Timing Array (EPTA), as well as the Parkes radio telescope of the Commonwealth Scientific and Industrial Research Organisation (CSIRO) Australia Telescope National Facility (ATNF) and the 26 m Mt Pleasant radio telescope operated by the University of Tasmania.

In particular, the observations of the Vela Pulsar have been secured by the Mt. Pleasant Radio Observatory. Data were collected at a central frequency of 1.4 GHz. Given the pulsar brightness, it is possible to extract a pulse Time of Arrival (ToA) about every 10 s, so that a total of 4098 ToAs are obtained for the time interval between 2007 February 26 (MJD 54,157) and 2008 March 23 (MJD 54,548), encompassing the whole time span of the *AGILE* observations. During this time interval, the pulsar experienced a small glitch (fractional frequency increment  $\Delta\nu_g/\nu \simeq 1.3 \times 10^{-9}$ ), which presumably happened around 2007 August 1 (with an uncertainty of  $\pm 3$  days due to the lack of observations around this period; see Section 6.3). Ephemeris for the pre- and postglitch time intervals were then separately calculated and applied to the gamma-ray folding procedure.

The observations of the Crab Pulsar have been provided by the telescopes of Jodrell Bank and Nançay. At Jodrell Bank, the Crab Pulsar has been daily observed from 2006 December 9 (MJD 54,078) to 2007 October 6 (MJD 54,379) and again from 2008 February 6 (MJD 54,502) to 2008 April 10 (MJD 54,566), which resulted in 334 ToAs. The observations were mainly performed at 1.4 GHz with the 76 m Lovell telescope, with some data also taken with the 12 m telescope at a central frequency of 600 MHz. The Nançay Radio Telescope (NRT) is a transit telescope with the equivalent area of a 93 m dish and observed at a central frequency of 1.4 GHz over the time interval between 2006 December 5 (MJD 54,074) and 2007 September 7 (MJD 54,350), producing 64 ToAs. A timing solution was

produced by joining the ToAs from the two telescopes and accounting for the phase shift that naturally ensues from data sets coming from different telescopes.

The observations of pulsar B1706–44 have been performed at the 64 m telescope at Parkes, in Australia, at the mean observing frequency of 1.4 GHz. They produced a total of 20 ToAs over the interval from 2007 April 30 (MJD 54,220) to 2008 Apr 6 (MJD 54,562), thus covering the whole *AGILE* observing time span for this target.

The timing of all pulsars is performed using the TEMPO2 software (Hobbs et al. 2006; Edwards et al. 2006). It first converts the topocentric ToAs to solar-system barycentric ToAs at infinite frequency<sup>27</sup> (using the Jet Propulsion Laboratory (JPL) DE405 solar system ephemeris<sup>28</sup>) and then performs a multiparameter least-square fit to determine the pulsar parameters. The differences between the observed barycentric ToAs and those estimated by the adopted timing model are represented by the so-called *residuals*. The procedure is iterative and improves with longer timescales of observations. An important feature developed by TEMPO2 is the possibility of accounting for the timing noise in the fitting procedure (see Section 4). This is particularly useful in timing the young pulsars; in fact, most of them suffer from quasi-random fluctuations (typically characterized by a very red noise spectrum) in the rotational parameters, whose origin is still debated. TEMPO2 corrects the effects of the timing noise on the residuals by modeling its behavior as a sum of harmonically correlated sinusoidal waves (see Equation (2) in Section 4) that is subtracted from the residuals.

The left panels (labeled as *prewhitening*) in Figure 2 report the timing residuals obtained over the data span of the radio observations without the correction for the timing noise, whereas the right panels (labeled as *whitened*) show the residuals after the application of the correction. The comparison between the panels in the two columns shows that this procedure has been very effective in removing the timing noise in Vela, Crab, and PSR B1706–44. The impact of this whitening procedure on the gamma-ray data analysis is discussed in Section 5.

Geminga is a radio-quiet pulsar whose ephemeris can be obtained from X-ray data. Following the demise of *CGRO*, Geminga was regularly observed with *XMM-Newton* in order to maintain its ephemeris for use in analyzing observations at other wavelengths. We analyzed all eight observations of Geminga (1E 0630+178, PSR J 0633+1746) taken with the X-ray (0.1–15 keV) cameras of *XMM-Newton* (Jansen et al. 2001) between MJD 52,368 and MJD 54,534 (2002 April–2008 March), with exposures in the range of 20–100 ks.

The data were processed using version 7.1.0 of the *XMM-Newton* Science Analysis Software (SAS) and the calibration files released in 2007 August. For the timing analysis, we could only use the pn data (operated in Small Window mode: time resolution 6 ms, imaging on a  $4' \times 4'$  field), owing to the inadequate time resolution of the MOS data. We selected only single and double photon events (patterns 0–4) and applied standard data screening criteria. Photon arrival times were converted to the solar system barycenter (SSB) using the SAS task *barycen*. To extract the source photons, we selected a circle of  $30''$  radius, containing about 85% of the source counts. Using standard folding and phase-fitting techniques, the source pulsations were clearly detected in all the observations. We

derived for Geminga the long-term spin parameters valid for the epoch range 52,369–54,534 MJD. Note that the absolute accuracy of the *XMM-Newton* clock is better than  $600 \mu\text{s}$  (Kirsch et al. 2004).

The Crab Pulsar is embedded in the Crab Nebula and represents about 10% of its flux in the hard X-ray band. Being a bright source with a relatively soft high-energy spectrum, the Crab pulsar is easily detected by SuperAGILE in less than one *AGILE* orbital revolution. Since the on-board time reconstruction of SuperAGILE (Feroci et al. 2007) is different from that of the GRID, as a crosscheck and test of the SuperAGILE timing performances, we processed the X-ray data of an on-axis observation of  $\sim 0.7$  days (54,360.7–54,361.4 MJD), corresponding to an effective exposure of  $\sim 41$  ks. In the analyzed data, the passages of *AGILE* in the SAA and intervals of source occultation by the Earth were excluded. The time entries in SuperAGILE event files are in the on-board time reference system (Coordinated Universal Time (UTC)) and were converted in Terrestrial Dynamical Time (TDT) before being processed and analyzed by the same procedures used for the GRID (see Section 4). A complete analysis of the X-ray observations of Crab with SuperAGILE is beyond the scope of this work; it will be presented in a future paper, as well as the search for the Crab pulsed signal in the *AGILE* mini-calorimeter data.

#### 4. GAMMA-RAY TIMING PROCEDURES

In this section, we will describe the timing procedures we have adopted. They have been implemented with two aims: to verify the timing performances of *AGILE* and to maximize the quality of the detection of the four targets.

*AGILE* on-board time is synchronized to UTC by the Global Positioning System (GPS) time sampled at a rate of 1 Hz. Arrival time entries in *AGILE* event list files are then corrected to TDT reference system at a ground segment level. In order to perform timing analysis, they also have to be converted to Barycentric Dynamical Time (TDB) reference and corrected for arrival delays at SSB. This conversion is based on the precise knowledge of the spacecraft position in the solar system frame. To match the instrumental microsecond absolute timing resolution level, the required spacecraft positioning precision is  $\lesssim 0.3$  km. This goal is achieved by the interpolation of GPS position samples extracted from telemetry packets. Earth position and velocity with respect to SSB are then calculated by JPL planetary ephemeris DE405. All the above barycentric corrections are handled by a dedicated program (implemented in the *AGILE* standard data reduction pipeline) on the event list extracted according to the criteria described in Section 2.

Pulsed signals in GRID gamma-ray data cannot be simply found by Fourier analysis of the photon SSB arrival times, since the pulsar rotation frequencies are 4–5 orders of magnitude higher than the gamma-ray pulsars typical count rates (10–100 counts/day). The determination of the pulsar rotational parameters in the gamma ray must then start from at least approximate knowledge of the pulsar spin ephemeris, provided by observations at other wavelengths.

Standard epoch folding is performed over a tridimensional grid centered on the nominal values of the pulsar spin frequency  $\nu_0$  and of its first- and second-order time derivatives,  $\dot{\nu}_0$  and  $\ddot{\nu}_0$ , as given by the assumed (radio or X-ray) ephemeris at their reference epoch  $t_0 = \text{PEPOCH}$ . The axes of the grid are explored with steps equal to  $1/T_{\text{span}}$ ,  $2/T_{\text{span}}^2$ , and  $6/T_{\text{span}}^3$  (all of them oversampled by a factor of 20), where  $T_{\text{span}}$  is the time

<sup>27</sup> Dispersion measure is obtained as part of a timing solution for Crab (DM=56.76(1)), Vela (DM=68.15(2)), and from Johnston et al. (1995) for B1706–44 (DM=75.69(5)).

<sup>28</sup> See <ftp://ssd.jpl.nasa.gov/pub/eph/export/DE405/de405.iom/>.

span of the gamma-ray data. For any assigned tern  $[\nu; \dot{\nu}; \ddot{\nu}]$ , the pulsar phase  $\Phi^*$  associated with each gamma-ray photon is determined by the expression

$$\Phi^* = \Phi_0 + \nu\Delta t + \frac{1}{2}\dot{\nu}\Delta t^2 + \frac{1}{6}\ddot{\nu}\Delta t^3, \quad (1)$$

where  $\Delta t = t - t_0$  is the difference between the SSB arrival time  $t$  of the photon and the reference epoch  $t_0$  of the ephemeris and  $\Phi_0$  is a reference phase (held fixed for all the sets). A light curve is formed by binning the pulsar phases of all the photons and plotting them in a histogram. Pearson's  $\chi^2$  statistic is then applied to the light curves resulting from each set of spin parameters, yielding the probabilities of sampling a uniform distribution. These probabilities  $\mathcal{P}(\nu; \dot{\nu}; \ddot{\nu})$  are then weighted for the number  $\mathcal{N}_{\text{st}}$  of steps over the grid, which has been necessary to reach the set  $[\nu; \dot{\nu}; \ddot{\nu}]$  starting from  $[\nu_0; \dot{\nu}_0; \ddot{\nu}_0]$ . The maximum value over the grid of  $\mathcal{S} = 1 - \mathcal{N}_{\text{st}}\mathcal{P}(\nu; \dot{\nu}; \ddot{\nu})$  finally determines which are the best gamma-ray rotational parameters for the target source in the surroundings of the given ephemeris. Of course, the higher the value of  $\mathcal{S}$ , the higher is the statistical significance of a pulsating signal. We note that this approach allows us to avoid any arbitrariness in the choice of the range of the parameters to be explored, which otherwise can affect the significance of a detection.

Due to the brightness of the sources discussed in this paper, period folding around the extrapolated pulsar spin parameters, obtained from publicly-available ephemerides (ATNF Pulsar Catalog,<sup>29</sup> Manchester et al. 2005; Jodrell Bank Crab ephemeris archive,<sup>30</sup> Lyne et al. 1993) or from recent literature, led us to firmly detect ( $> 5\sigma$ ) the pulsations for all the four targets with a reasonable number of trials ( $\lesssim 1000$ ). However, for three of them (Crab, Vela, and PSR B1706–44), the best gamma-ray spin period fell outside the  $3\sigma$  uncertainty range of the adopted radio ephemeris, and the detection significance  $\mathcal{S}$  resulted lower than that derived using contemporary timing solutions (accounting for the effects of timing noise and/or occasional glitches), provided by dedicated radio observation campaigns (see Section 3). As expected, for steady and older pulsars, such as Geminga, the availability of contemporary rotational parameters turned out to be less important; even by using a few-year-old ephemeris, the pulsed signal could be detected within only  $< 100$  period search trials around the extrapolated X-ray timing solutions.

An additional significant improvement (see Section 5) in the detection significance has been obtained by also accounting for the pulsar timing noise in the folding procedure. This exploits a tool of TEMPO2 (Hobbs et al. 2006; Edwards et al. 2006), namely the possibility of fitting timing residuals with a polynomial harmonic function  $\Delta R$  in addition to standard positional, rotational, and (when appropriate) binary parameters (Hobbs et al. 2004):

$$\Delta R(\Delta t) = \sum_{k=1}^N a_k \sin(k\omega\Delta t) + b_k \cos(k\omega\Delta t), \quad (2)$$

where  $N$  is the number of harmonics (constrained by precision requirements on radio timing residuals, as well as by the span and the rate of the radio observations),  $a_k$  and  $b_k$  are the fit parameters (i.e., the WAVE terms in TEMPO2 ephemeris files), and  $\omega = 2\pi(T_{\text{radio}}(1 + 4/N))^{-1}$  is the main frequency (i.e., WAVE<sub>OM</sub> in TEMPO2 ephemeris files) related to the radio data time span  $T_{\text{radio}}$ .

If the spin behavior of the target is suitably sampled, the harmonic function  $\Delta R$  can absorb the rotational irregularities of the source, in a range of timescales ranging from  $\sim T_{\text{radio}}$  down to about the typical interval between radio observations. As an example, the peak-to-peak amplitude of the  $\Delta R$  fluctuations for Crab related to the radio monitoring epochs (54,074–54,563 MJD) covering our *AGILE* observations is of the order of  $\sim 1$  ms, corresponding to a phase smearing of  $> 0.03$ , a value significantly affecting the time resolution of a  $> 50$ -bin light curve. Under the assumption that the ToAs of the gamma-ray photons are affected by timing noise like in the radio band, gamma-rays folding can properly account for  $\Delta R$ , extending Equation (1) to

$$\Phi = \Phi^* + \left( \nu + \dot{\nu}\Delta t + \frac{1}{2}\ddot{\nu}\Delta t^2 \right) \Delta R \simeq \Phi_0 + \nu\Delta t \left( 1 + \frac{\Delta R}{\Delta t} \right) + \frac{1}{2}\dot{\nu}\Delta t^2 + \frac{1}{6}\ddot{\nu}\Delta t^3. \quad (3)$$

As reported in Section 5, this innovative phasing technique significantly improves the gamma-ray folding accuracy for young and energetic pulsars, especially when using long data spans, like those of the *AGILE* observations. Of course, the implementation of this procedure requires radio observations covering the time span of the gamma-ray observations making the radio monitoring described in Section 3 all the more important.

## 5. TIMING CALIBRATION TESTS AND RESULTS

In order to verify the performances of the timing analysis procedure described in Section 4, a crucial parameter to check is the difference between pulsar rotation parameters derived from radio, X-ray, and gamma-ray data. Figure 3 shows the *AGILE* period search result for the Crab pulsar (corresponding to the MJD 54,305–54,406 observations, significantly affected by timing noise, as shown in Figure 2). The implementation of the folding method described in Section 4, including timing noise corrections as given by Equation (3), allowed for a perfect match between the best period resulting from gamma-ray data and the period predicted by the radio ephemeris with discrepancies  $\Delta P_{\text{Crab}} \sim 3 \times 10^{-12}$  s, comparable with the period search resolution  $r_{\text{Crab}} \sim 2 \times 10^{-12}$  s. This also represents an ultimate test for the accuracy of the on-board *AGILE* Processing and Data Handling Unit (PDHU; Argan et al. 2004), time management (clock stability in particular), and on-ground barycentric time correction procedure. Standard folding without the  $\Delta R$  term implies radio-gamma period discrepancies one order of magnitude higher ( $\Delta P_{\text{Crab}} \sim 4 \times 10^{-11}$  s). Moreover, it also lowers the statistical significance of the detection and effective time resolution of the light curve. For the Crab, the value of the Pearson's  $\chi^2$  statistic introduced in Section 4 (we quote reduced  $\chi^2$  values) goes from  $\sim 6.3$  (when using the  $\Delta R$  term) down to  $\sim 4.2$  (ignoring the  $\Delta R$  term) when folding the data into a 50-bin light curve (see Figure 4). Obviously, ignoring timing noise in the folding process would yield discrepancies (and light-curve smearing) that are expected to grow when considering a longer observing time span. Thus, the contribution of timing noise should be considered both in high-resolution timing analysis and in searching for new gamma-ray pulsars. The same analysis applied to Vela and PSR B1706–44—much less affected than Crab by timing noise in the considered data span—led to similar results for the period discrepancies ( $\Delta P_{\text{Vela}} \sim 8 \times 10^{-12}$  s and  $\Delta P_{\text{B1706}} \sim 3 \times 10^{-11}$  to be compared

<sup>29</sup> See <http://www.atnf.csiro.au/research/pulsar/psrcat/>.

<sup>30</sup> See <http://www.jb.man.ac.uk/~pulsar/crab.html>.

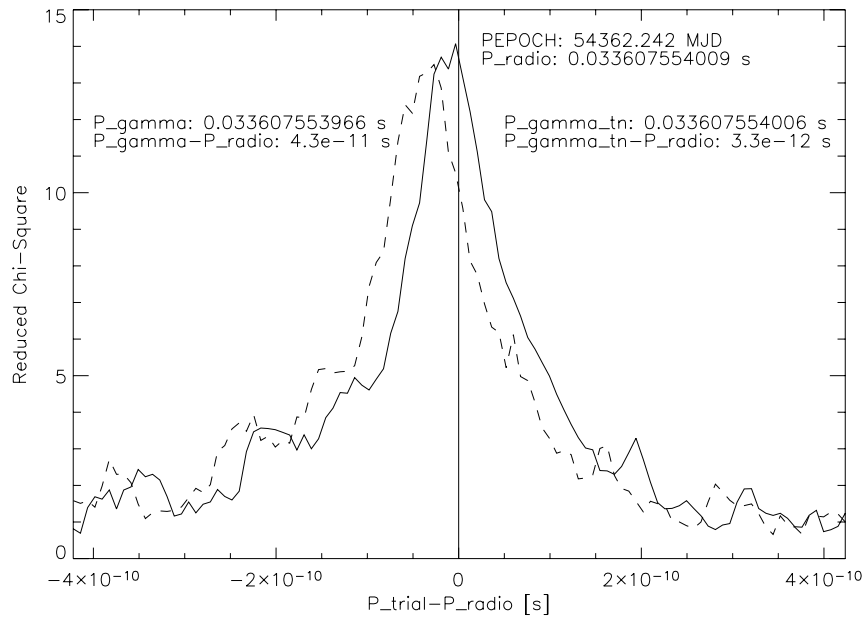


**Figure 3.** Period search result for the Crab pulsar (period trials vs.  $\chi^2$  Pearson statistics). The radio period (vertical line at  $P_{\text{trial}} - P_{\text{radio}} = 0$ ) is 33.607554009(4) ms ( $PEPOCH = 54,362.242$  MJD). Dashed line is obtained from standard folding period trials, while continuous line is from the folding technique accounting for timing noise (see Section 3). The new method allow us to perfectly match the radio period in gamma rays ( $P_{\text{gamma\_tn}} - P_{\text{radio}} \sim 3 \times 10^{-12}$  s). It is worth noting that in the considered data span (54,305–54,406 MJD), the period search resolution ( $r_{\text{Crab}} \sim 2 \times 10^{-12}$  s) is about an order of magnitude higher than the  $1\sigma$  error on the radio period.

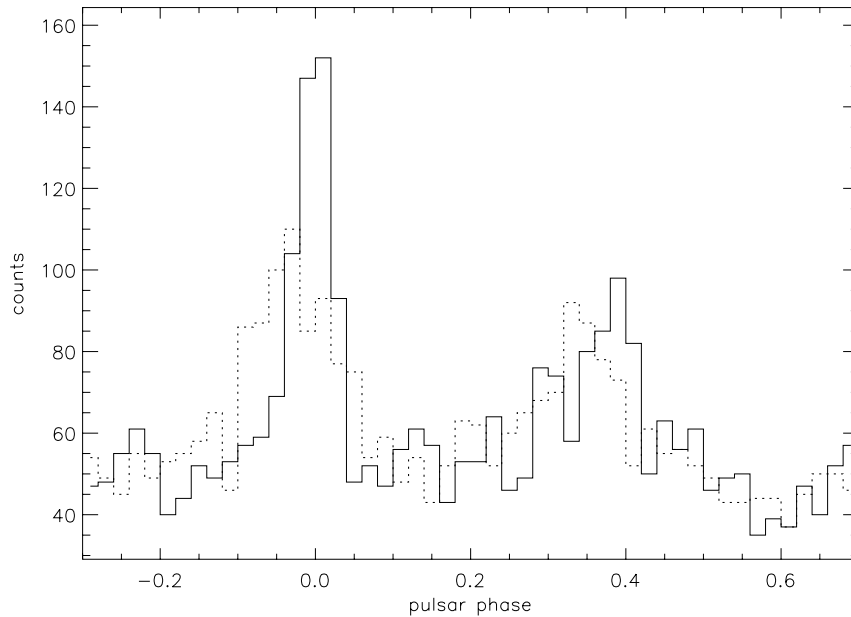


**Figure 4.** Crab light curve (50 bin) corresponding to the data span 54,305–54,406 MJD, obtained by folding including  $\Delta R$  terms, compared with that obtained neglecting timing noise (dashed line). In observing periods strongly affected by timing noise, the smearing effects reduce detection significance and observed pulsed counts (see text).

with the period search resolutions  $r_{\text{Vela}} \sim 9 \times 10^{-12}$  s and  $r_{\text{B1706}} \sim 2 \times 10^{-11}$  s, respectively).

For the radio-quiet Geminga pulsar, we used X-ray ephemeris obtained from *XMM-Newton* data (see Section 3) as a starting point for the period search. Due to the stability of the spin parameters of this relatively old pulsar, not significantly affected by timing noise, *WAVE* parameters are not required for the folding process. The X-ray versus gamma-ray period discrepancy was  $\Delta P_{\text{Gem}} \sim 9 \times 10^{-12}$  s, whereas  $r_{\text{Gem}} \sim 7 \times 10^{-11}$  s. We here note that the frequency resolution  $1/T_{\text{span}} \sim 10^{-7}$  Hz of

*AGILE* is about one order of magnitude better than that corresponding to a single *XMM-Newton* exposure (lasting  $\lesssim 100$  ks), but the few-year long X-ray data span implies an overall much better effective resolution of  $1/T_{\text{XMM}} \sim 5 \times 10^{-9}$  Hz for the *XMM-Newton* data.

The resulting gamma-ray light curves, covering different energy ranges for the four pulsars, are shown in Figures 5–8. The pulsed flux was computed considering all the counts above the minimum of the light curve, using the expression  $PF = C_{\text{tot}} - nN_{\text{min}}$  and its associated error  $\sigma_{\text{PF}} = (C_{\text{tot}} + n^2\sigma_{N_{\text{min}}}^2)^{1/2} \simeq$

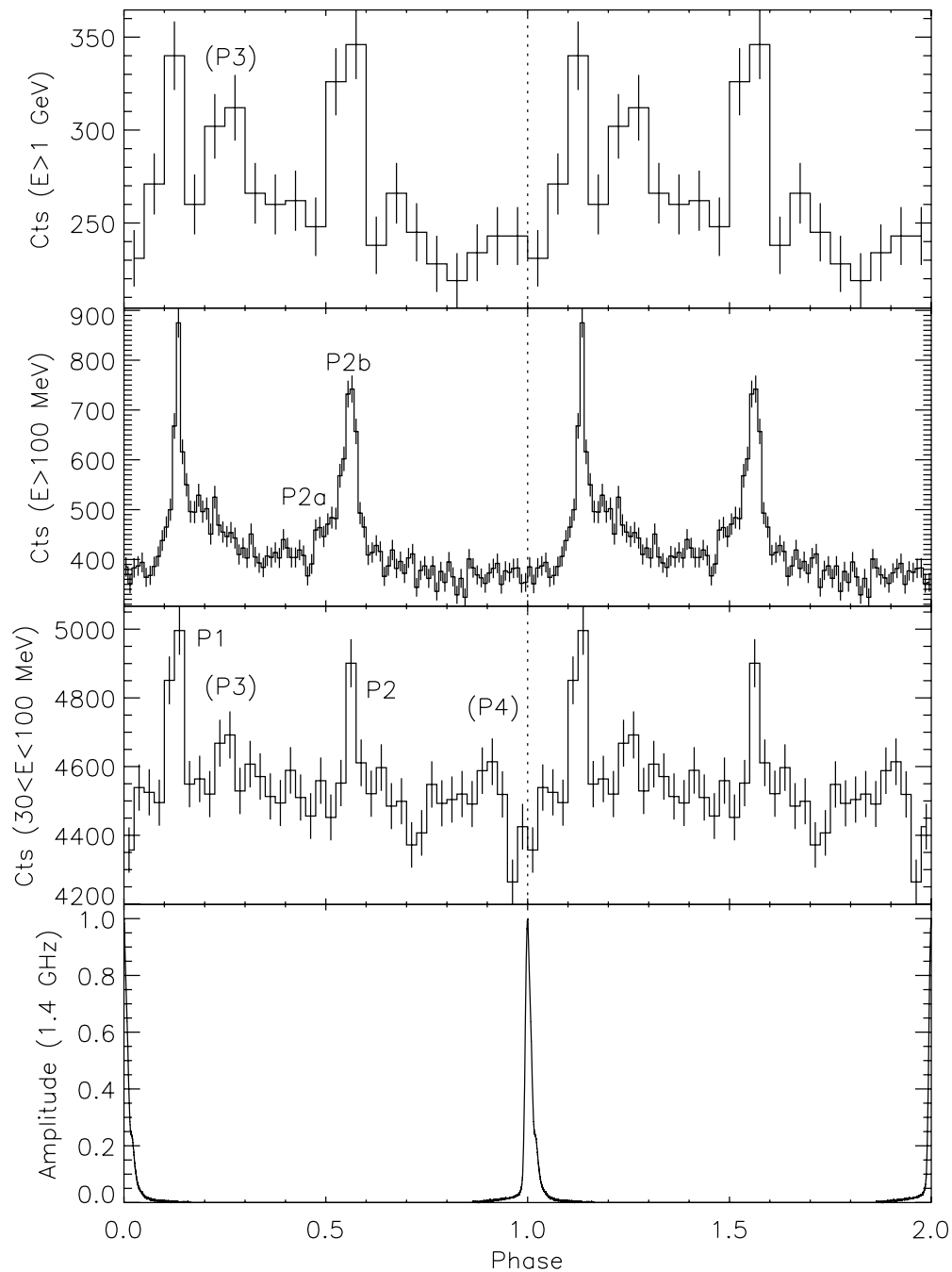


**Figure 5.** Vela pulsar light curves ( $P \sim 89.3$  ms) for different energy bands ( $E < 100$  MeV, 40 bins, resolution:  $\sim 2.2$  ms;  $E > 100$  MeV, 100 bins, resolution:  $\sim 0.9$  ms;  $E > 1$  GeV, 20 bins, resolution:  $\sim 4.5$  ms; G+L class events) obtained by integrating all available postglitch data (54,320–54,561 MJD). The radio ephemeris and the 8192 bin light curve (bottom panel) are obtained by the analysis of  $\sim 4100$  ToAs observed at Mt. Pleasant Radio Observatory in Tasmania (radio observation interval 54,157–54,548 MJD).

$n(N_{\min})^{1/2}$ , where  $C_{\text{tot}}$  are the total counts,  $n$  is the number of bins in the light curve, and  $N_{\min}$  are the counts of bin corresponding to the minimum. This method is “bin dependent,” but reasonable different choices of both the number of bins (i.e.,  $n > 10$ ) and the location of the bin center (10 trial values were explored for each choice of  $n$ ) do not significantly affect the results. Several models (polar cap, slot gap) predict that gamma-ray pulsar emission is present in all phases. When enough count statistics will be available, (e.g.,  $\sim 10,000$  counts for the Crab pulsar), it will be possible to estimate the unpulsed emission (due to the pulsar plus a possible contribution from the pulsar wind nebula) by considering the difference among the total source

fluxes obtained by a likelihood analysis on the images and the pulsed flux estimated with the above method.

Pulsed counts and related Pearson statistics for the four pulsars are reported in Table 2 (for the standard event extraction parameters as in Table 1). The resulting fluxes (pulsed counts/exposure) are consistent with those reported in the EGRET Catalogue (Hartman et al. 1999). We note that source-specific extraction parameters (event class, source position in the FOV, energy band, etc.), which maximize reduced  $\chi^2$ , can significantly improve detection significance. For example, including only the event class G in the timing analysis of Crab and Geminga halves the number of pulsed counts while doubling the  $\chi^2$  values.

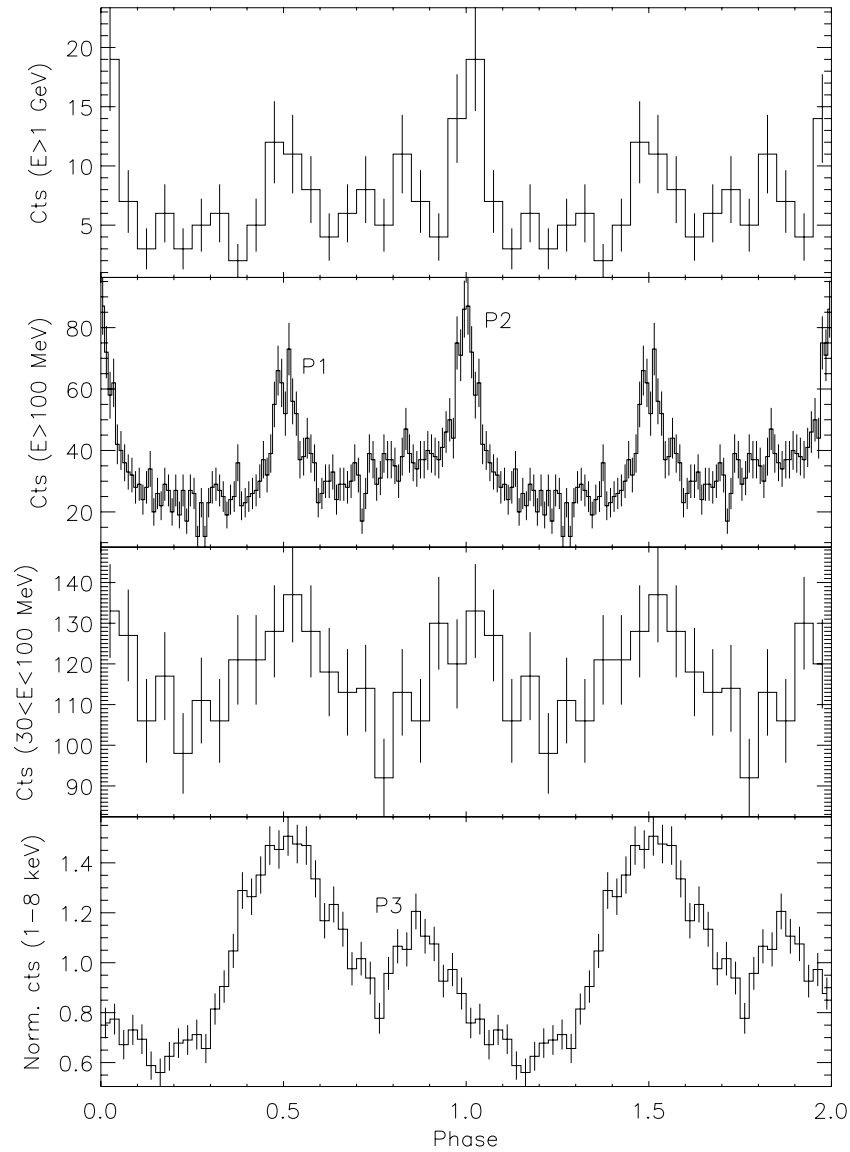


**Figure 6.** Geminga light curves ( $P \sim 237.1$  ms) for different energy bands ( $E < 100$  MeV, 20 bins, resolution:  $\sim 11.8$  ms;  $E > 100$  MeV, 100 bins, resolution:  $\sim 2.4$  ms;  $E > 1$  GeV, 20 bins, resolution:  $\sim 11.8$  ms; G class events). The X-ray ephemeris and the 1–8 keV 40 bin light curve (bottom panel) are obtained by the analysis of *XMM-Newton* data (observation interval 52,369–54,534 MJD).

Despite the very satisfactory matching of the pulsar spin parameters found in radio (or X-ray) and gamma-ray (supporting the clock stability and the correctness of the SSB transformations), possible systematic time shifts in the *AGILE* event lists could be, in principle, affecting phasing and must be checked. For example, a hypothetical constant discrepancy of  $t_{\text{err}}$  of the on-board time with respect to UTC would result in a phase shift  $\Phi_{\text{err}} = (t_{\text{err}} \bmod P)/P$ , where  $P$  is the pulsar period. The availability of radio observations bracketing the time span of the gamma-ray observations (or of X-ray observations very close to the gamma-ray observations for the case of Geminga) also allowed us to perform accurate phasing of multiwavelength light curves. In doing that, radio ephemeris reference epochs were set to the main peak of radio light curves at phase  $\Phi_{\text{peak}} = 0$ . In view of Equations (2) and (3), this is achieved by setting  $\Phi_0 = -\nu \sum_{k=1}^N b_k$  (typically,  $\Phi_0 < 10^{-2}$ ). We found that the phasing of the *AGILE* light curves of the four pulsars (radio/X-rays/gamma-ray peaks phase separations) is consistent with EGRET measurements (Fierro et al. 1998; Thompson

et al. 1996; Jackson & Halpern 2005; see Section 6 for details) implying no evidence of systematic errors in absolute timing with an upper limit  $t_{\text{err}} < 1$  ms.

Comparison with the SuperAGILE light-curve peak (see Section 3) is also interesting (SuperAGILE on-board time processing is more complex than that of the GRID). The Crab SuperAGILE light curve (Figure 7) was produced with the same folding method reported in Section 4, yielding  $63,700 \pm 8700$  pulsed counts ( $\sim 3\%$  of the total counts including background). Inspection of Figure 7 shows that the X-ray peaks are aligned with the  $E > 100$  MeV data within  $\Delta\phi \sim 400 \mu\text{s}$  (a value obtained by fitting the peaks with Gaussians), providing an additional test of the *AGILE* phasing accuracy.

The effective time resolution of *AGILE* light curves results from the combination of the different steps involved in the processing of gamma-ray photon arrival times. The on-board time tagging accuracy is a mere  $\sim 1 \mu\text{s}$ , with negligible dead time. For comparison, the corresponding EGRET time tagging accuracy was  $\sim 100 \mu\text{s}$ . The precise GPS spacetime positioning

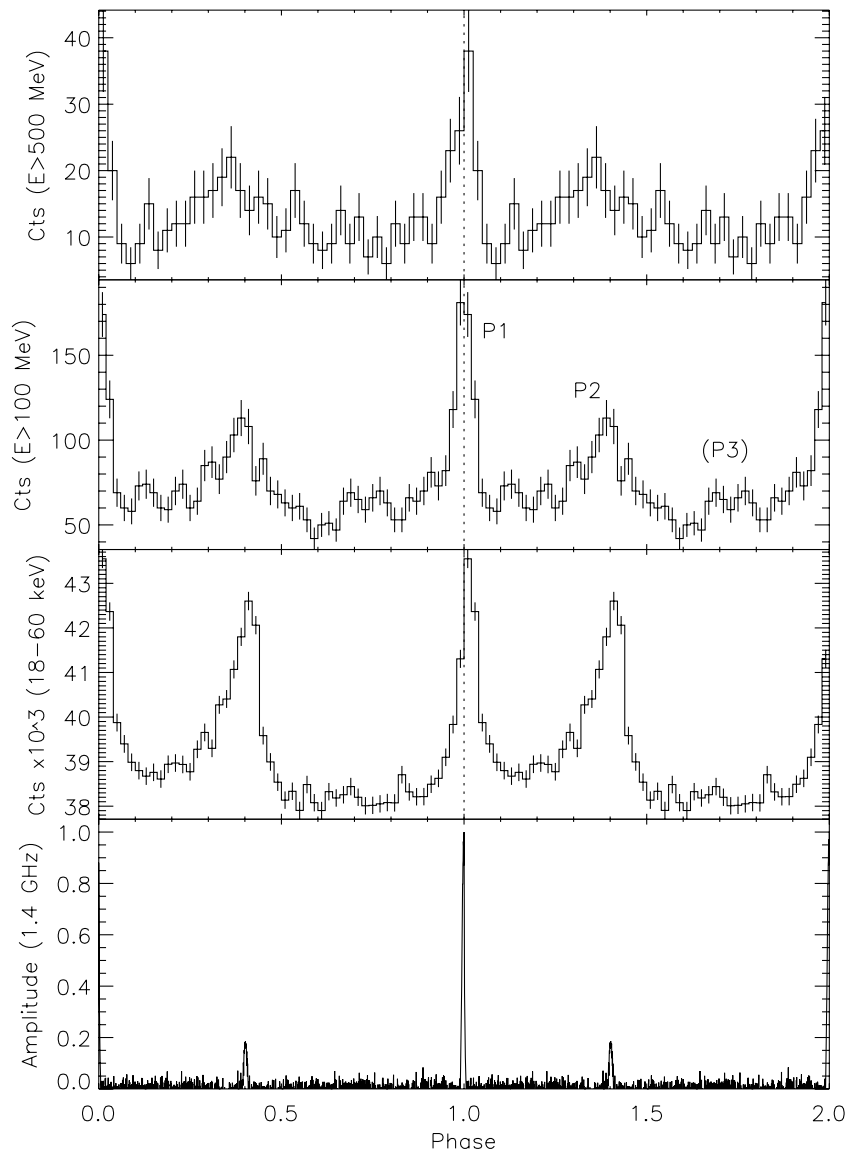


**Figure 7.** Crab pulsar light curves ( $P \sim 33.1$  ms) for different energy bands ( $E > 100$  MeV, 50 bins, resolution:  $\sim 0.7$  ms;  $E > 500$  MeV, 40 bins, resolution:  $\sim 0.8$  ms; G class events) obtained by integrating all available data presented in Table 1. The X-ray (18–60 keV) SuperAGILE 50-bin light curve is obtained from a  $\sim 41$  ks observation taken at  $\sim 54,361$  MJD. The radio ephemeris and the 2048 bin light curve (bottom panel) are obtained by the analysis of 334 ToAs observed by Jodrell Bank and Nançay radio telescopes (observation interval 54,078–54,566 MJD).

of the *AGILE* spacecraft (Argan et al. 2004) allows for the transformation from UTC to the SSB time frame (TDB) with only a moderate loss ( $\lesssim 10 \mu\text{s}$ ) of the intrinsic instrumental time accuracy. The innovative folding technique described in Section 4, accounting for pulsar timing noise, also reduces smearing effects in the light curves, fully exploiting all the information from contemporary radio observations. In summary, the effective time resolution of the current *AGILE* pulsar light curves (and then multiwavelength phasing accuracy assuming  $t_{\text{err}} = 1 \mu\text{s}$ ) is mainly limited by the available count statistics and can be estimated by

$$\Delta t = \frac{P}{N} = \frac{\sigma^2(C_p + 2B)}{C_p^2}, \quad (4)$$

where  $P$  is the pulsar period,  $N$  is the number of bins in the light–curve histogram,  $\sigma$  is the S/N,  $C_p$  are the pulsed counts, and  $B$  are the background counts. In order to keep the average S/N of light–curve bins (during the

on–pulse phase) at a reasonable level ( $> 3\sigma$ ), the resulting effective time resolution is constrained to 200–500  $\mu\text{s}$ . At present, the best effective time resolution ( $\sim 200 \mu\text{s}$ ) is obtained for the 400 bin light curve of Vela (G+L class selection) although a 100 bin light curve (Figure 5) is better suited to study pulse shapes and to search for possible weak features. The effective time resolution will obviously improve with exposure time  $\Delta t \propto T_{\text{exp}}^{-1}$ , and a resolution of  $\lesssim 50 \mu\text{s}$  is expected after 2 years of *AGILE* observations of Vela.

## 6. DISCUSSION

With about 10 years since the last gamma-ray observations of Crab, Vela, Geminga (Fierro et al. 1998), and B1706–44 (Thompson et al. 1996) by CGRO, the improved time resolution of *AGILE* and the much longer observation campaigns in progress now offer the possibility of both to search for new features in the shape of the light curves of these gamma-ray pulsars and to investigate the possible occurrence of variations in the gamma-ray pulsed flux parameters.

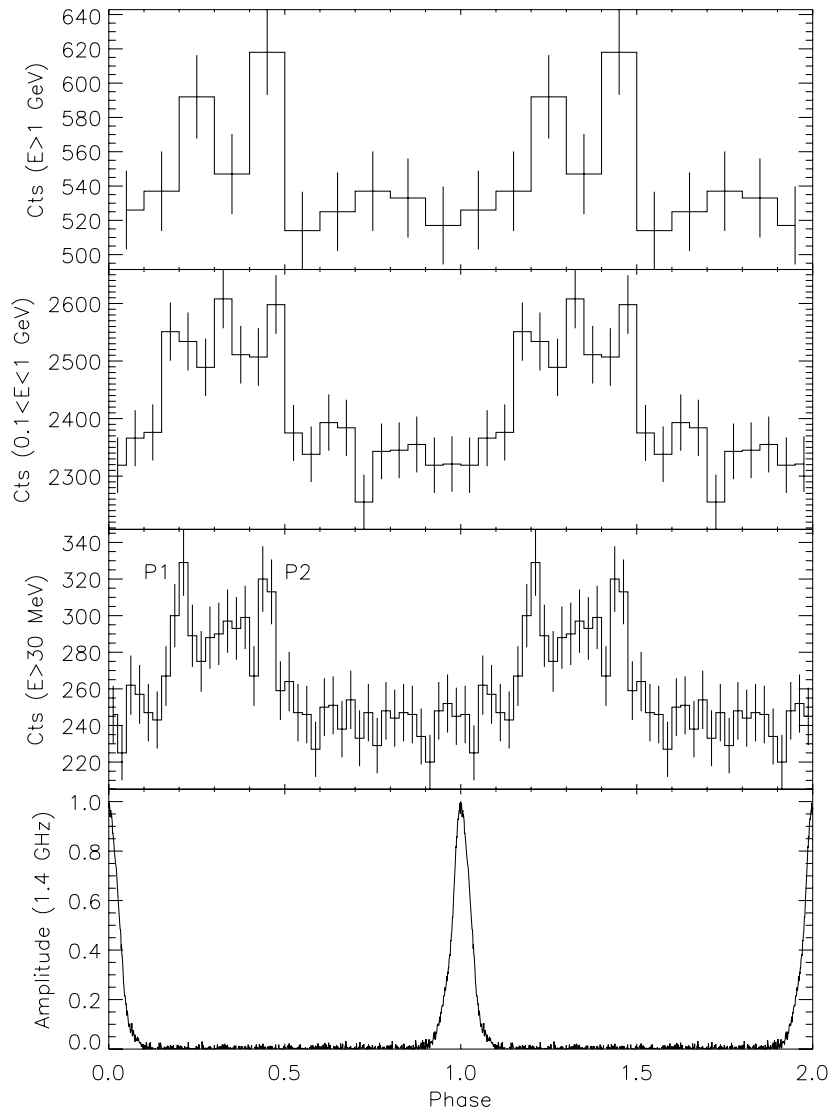


**Figure 8.** PSR B1706–44 light curves ( $P \sim 102.5$  ms) for different energy bands ( $E > 30$  MeV, G class events, 40 bins, resolution:  $\sim 2.6$  ms;  $0.1 < E < 1$  GeV, G+L class events, 20 bins, resolution:  $\sim 5.1$  ms;  $E > 1$  GeV, G+L class events, 10 bins, resolution:  $\sim 10.2$  ms) obtained by integrating all available data presented in Table 1. The radio ephemeris and the 1024 bin light curve (bottom panel) are obtained by the analysis of 20 ToAs observed by Parkes radio telescope (observation interval 54,220–54,562 MJD).

After nine months of observations in the frame of the SVP (2007 July–November) and of the Scientific Pointing Program AO 1 (pointings 1–7, 2007 December 1–2008 April 10), *AGILE* reached an exposure ( $E > 100$  MeV) of the Vela region  $\gtrsim 10^9$  cm<sup>2</sup> s ( $\sim 10,000$  pulsed counts from Vela), comparable with that of the 9 year life of EGRET (although *AGILE* data have a higher residual particle background), and an even better exposure ( $1.5 \times 10^9$  cm<sup>2</sup> s) in the core region of the Galactic Plane ( $l = 310^\circ$ – $340^\circ$ ) corresponding to the Southern Hemisphere. In fact, *AGILE* observed  $\sim 2400$  pulsed counts from PSR B1706–44 up to date, a factor of 1.5 better count statistics than EGRET for this source. For Crab and Geminga, an exposure level comparable with that obtained by EGRET will be reached at the end of the AO 1 pointing number 15 in the Anti-Center region (2008 October).

### 6.1. The gamma-ray light curves

The plots shown in Figures 5–8 allow us to start assessing new features in gamma-ray pulsar light curves. Narrower and better-resolved main peaks are revealed, together with previ-

ously unknown secondary features, to be confirmed when more count statistics (and an improved particle background filtering) will be available.

The Vela light curves for different energy bands are shown in Figure 5. A Gaussian fit to the Vela main peak (P1) at  $E > 100$  MeV provides a FWHM of  $0.018 \pm 0.002$  centered at  $\phi = 0.1339 \pm 0.0007$  in phase consistent with the EGRET observations (Kanbach et al., 1994). The apex of the main peak is resolved by *AGILE* with a width of  $\sim 0.8$  ms and its apparent trail ( $\phi = 0.13$ – $0.3$ ) could be due to the occurrence of one or more secondary peaks. In fact, marginal evidence of a relatively narrow lower peak (P3) at  $\phi \sim 0.25$  is present in the  $E < 100$  MeV ( $3.3\sigma$  fluctuation with respect to the average interpulse rate) and in the  $E > 1$  GeV ( $3.8\sigma$ ) light curves. P3 is located at the phase of the optical peak 1, and also at the phase of a bump predicted in a two-pole caustic model (Dyks et al. 2004), due to overlapping field lines from opposite poles near the light cylinder. In the outer gap model, this bump is the first peak in the light curve, and also comes from very near the light cylinder. The peak at  $\phi = 0.5$ – $0.6$  (P2) in the  $E > 100$  MeV light curve cannot be satisfactorily fitted with

a single Gaussian or a Lorentzian curve ( $\chi_r^2 > 3$ ), due the possible presence of a bump at  $\phi \sim 0.5$  (P2a). A fit with two Gaussians provides  $\phi = 0.560 \pm 0.001$  (FWHM  $0.031 \pm 0.003$ ) and  $\phi = 0.49 \pm 0.01$  for the phases of the major peak (P2b) and lower peak apexes (P2a), respectively. The phase separation between the main gamma-ray peaks  $\Delta\phi = 0.426 \pm 0.002$ , as well as that between the gamma-ray and the radio peak, is unchanged since EGRET observations (Kanbach et al. 1994; Ramanamurthy et al. 1995). In the  $E < 100$  MeV band, a secondary peak+valley structure (P4) appears at  $\phi \sim 0.9$  ( $\sim 4\sigma$  level). It is worth noting its symmetric position around the radio peak with respect to the main peak (P1) and a possible correlation of P4 with features seen in the X-ray light curves (Manzali et al. 2007); P4 also coincides with peak number 3 of the *Rossi X-Ray Timing Explorer (RXTE)* light curve (Harding et al. 2002).

Geminga shows an  $E > 100$  MeV light curve (Figure 6) with properties similar to those of Vela. Apart from the major peaks P2 ( $\phi = 0.999 \pm 0.002$ , FWHM  $0.062 \pm 0.008$ ) and P1 (with apex  $\phi = 0.507 \pm 0.004$ , FWHM  $0.08 \pm 0.01$ ), secondary peaks are seen trailing P1 and leading P2: the main peak's P2 leading trail ( $\phi = 0.8$ – $1$ ) could be possibly associated with unresolved multiple peaks while P1 displays a “bump” at  $\phi \sim 0.55$ – $0.6$ . P1 seems to be characterized by a double structure: a fit with a simple Gaussian yields  $\chi_r^2 \sim 1.2$  to be compared with a double Gaussian model providing  $\chi_r^2 < 1$ . This feature still seems present even considering different observation blocks separately. The main-peak separation ( $\Delta\phi = 0.508 \pm 0.007$  at  $E > 100$  MeV) is greater than the value obtained for Vela, and it decreases slightly with energy. The 2–10 keV X-ray light curve shows a peak (P3) in correspondence with a possible excess in the hard gamma-ray band and a broad top-hat-shaped feature partially overlapping in phase with P1.

The Crab light curve for  $E > 100$  MeV (Figure 7) shows a previously-unknown broad feature at  $\phi = 0.65$ – $0.8$  (P3), in addition to the main peaks P1 and P2 ( $\phi_{P1} = 0.999 \pm 0.002$ , FWHM  $0.054 \pm 0.005$ ;  $\phi_{P2} = 0.382 \pm 0.008$ , FWHM  $0.14 \pm 0.04$ ). The probability of P3 being a background fluctuation is of  $\sim 10^{-4}$  ( $3.7\sigma$ ). P2 could be possibly resolved in two subpeaks in future longer observations. P3 is coincident with the feature HFC2 that appears in the radio profile above 4 GHz (Moffett & Hankins 1996). From the polarization of this component, Moffett & Hankins (1999) suggested that this peak may come from a lower emission altitude, near the polar cap. P3 is actually at a phase that could plausibly come from low-altitude cascades in the slot gap model (Muslimov & Harding 2004, Figure 2), the pairs which may also cause the HFC2 radio component(s), while P1 and P2 come from the high-altitude slot gap.

According to the observations of SAS-2, COS B, and *CGRO/EGRET*, the ratio P2/P1 of the main-peak intensities could present a variability pattern (possibly ascribed to the nutation of the neutron star) that can be fitted with a sinusoid with a period of  $\sim 13.5$  years (Kanbach 1990; Ramanamurthy et al. 1995) although this is not required by EGRET data alone (Tompkins et al. 1997). We observed a P2/P1 intensity ratio  $0.66 \pm 0.10$  in good agreement with the value of  $\sim 0.59$  predicted for 54,350 MJD (for the energy range of 50 MeV–3 GeV). Unfortunately, our P2/P1 value is similar—within the errors—to the EGRET determination ( $\sim 0.5$ ): then an unambiguous assessment of the origin of this possible phenomenology will require measurements close to the epoch (56,150 MJD) corresponding to the predicted maximum or the intensity ratio P2/P1 ( $\sim 1.4$ ). Variability should also be

invoked to explain the possible detection of P3, which was never seen before in the EGRET database in spite of an overall exposure comparable with that reached by *AGILE* so far. We note that the main-peak intensity ratios computed for Vela (P2/P1 =  $0.91 \pm 0.07$ ) and Geminga (P2/P1 =  $0.8 \pm 0.1$ ) do not yield evidence of significant variations with respect to past observations (Ramanamurthy et al. 1995).

The *AGILE* light curves of PSR B1706–44 are shown in Figure 8. The broadband light curve ( $E > 30$  MeV) clearly shows two peaks ( $\phi_{P1} = 0.211 \pm 0.007$ ,  $\phi_{P2} = 0.448 \pm 0.005$ ) bracketing considerable bridge emission (contributing to  $> 50\%$  of the pulsed counts) while in the 0.1–1 GeV range, the peaks cannot be discerned from the bridge emission and the pulsar profile presents an unresolved broad ( $\Delta\phi = 0.3$ – $0.4$ ) single peak. PSR B1706–44 is a young ( $\sim 2 \times 10^4$  yr) and energetic ( $3.4 \times 10^{36}$  erg s $^{-1}$ ) 102.5 ms pulsar (Johnston et al. 1992) with emission properties similar to Vela (Becker & Pavlov 2002). Double-peaked PSR B1706–44 is then in fact “Vela-like” not only energetically, but also with respect to the offset between the maxima of the high energy and the radio profiles, with neither of the two gamma-ray narrow pulses aligned to the radio peak.

*AGILE* allowed for a long monitoring of gamma-ray pulsar light-curve shapes. We carefully looked for possible light-curve variations by Kolmogorov–Smirnov (K–S) tests (two-dimensional K–S test; Peacock 1983; Fasano & Franceschini 1987). For each pulsar, different gamma-ray light curves (with 10, 20, and 40 bins) were obtained by grouping a contiguous data set and requiring at least 30 counts/bin (300–1000 counts for each light curve). Each light curve was compared with each other and with the average shape corresponding to the entire data set by the K–S test. No pulse-shape variation was detected with a significance  $> 3\sigma$  on timescales ranging from 1 day (Vela) to few months (Crab, Geminga, and PSR B1706–44).

## 6.2. Implications for the Emission Models

Pulsars derive their emitting power from rotational energy loss owing to the relativistic acceleration (up to the Lorentz factor  $\Gamma \sim 10^5$ – $10^7$ ) of charged particles by very high electric potentials induced by the rotating magnetic fields. The charge density that builds up in a neutron star magnetosphere is able to short out the electric field parallel to the magnetic field everywhere except a few locations of non-force-free “gaps.” It is unclear whether these acceleration regions can form in the strong field near ( $\lesssim 1$  stellar radii) the neutron star surface (polar cap/low-altitude slot gap model: Daugherty & Harding 1996 and Muslimov & Harding 2003; high-altitude slot gap model: Muslimov & Harding 2004 and Harding et al. 2008), in the outer magnetosphere near the speed of light cylinder (outer gap model: Cheng et al. 1986; Romani 1996; Hirotani & Shibata 2001; Takata & Chang 2007), or even beyond in the wind zone (Pétri & Kirk 2005).

In polar cap/low-altitude slot gap models, gamma rays result from magnetic pair cascades induced by curvature or inverse-Compton photons. The spectrum is dominated by synchrotron radiation of pairs at lower energies ( $\lesssim 1$  GeV) and by curvature radiation at higher energies ( $> 1$  GeV). In the high-altitude slot gap, gamma rays result from curvature radiation and synchrotron radiation of primary electrons (no cascade). In outer gap models, gamma rays result from photon–photon pair cascades induced by curvature radiation. The spectrum is dominated by pair synchrotron radiation below 20 MeV, curvature radiation above 20 MeV, and inverse Compton at 1–10 TeV.

The size and spectrum of the emitting regions are then directly related to the intensity and location in the magnetosphere of the accelerating electric fields. Strong fields imply thin accelerator gaps, while weaker fields are associated with thick gaps: the acceleration zone grows bigger as the particle must accelerate over a larger distance to radiate pair-production photons. On an observational point of view, it is in turn expected that acceleration gap sizes are related to the width of light-curve peaks. The highly relativistic particles emit photons at very small ( $\sim 1/\Gamma$ ) angles to the open magnetic field lines. The theoretical width of a light-curve peak associated with an infinitely small gap would then be  $\Delta t = P/(2\pi\Gamma)$ , a value typically smaller than  $1 \mu\text{s}$ . Therefore, the width of the apex of the peak can be related to the core gap size. For example, the  $\Delta t \sim 800 \mu\text{s}$  width of the Vela pulsar peak (P1) resolved by *AGILE* implies a projected gap core width of  $\sim 1 \text{ km}$  for a gap height of  $\sim 1$  stellar radii. Broader peaks as P2 and P3 in the Crab light curve instead involve a magnetospheric region, tens of kilometers long. The relation of the width of the peaks to the acceleration gap size works for the low-altitude emission models but is complicated by relativistic effects (aberration, retardation) in the high-altitude emission models, where the peaks are formed by caustics (Dyks & Rudak 2003). The peak widths will still depend on the width of the acceleration (outer or slot) gap, but one must perform a comparison with detailed models to constrain the physical size of the gap.

The likely presence of multiple contiguous peaks as P2a-b in the Vela light curve, P1 in Geminga, and possibly within the wide P2 broad peak in Crab could be related to short-term oscillation of gap locations. Light-curve variations on timescales of  $\gtrsim 1$  day are anyway excluded by the K-S tests described above. Alternatively, the apparent superimposition of different gaps placed at different heights in the magnetosphere could be another plausible explanation for multiple-contiguous peaks, while the hypothesis of jumps in the strength of acceleration electric fields would lack evident physical justification. In general, the presence of multiple (contiguous or not) structures in the light curves is difficult to fit in a scenario alternatively involving polar cap, outer gap, or wind zone models exclusively. The particle acceleration may well be simultaneously occurring in all the regions predicted by these models. Indeed, a three-peak light curve can still be explained invoking polar cap gaps alone provided that both polar caps can cross the line of sight (LOS).

Wherever in the magnetosphere a gap can form, a multifrequency emission may occur along a hollow cone (due to magnetosphere symmetries) or any other suitable surface: light-curve peaks are generated when the viewing angle from any given location on this surface to the observer also crosses the gap. The pulse spectrum slope depends on the accelerating field as well as on the magnetic fields, which strongly affect the synchrotron emission efficiency and the pair attenuation along the cascade path: the stronger the magnetic field is, the steeper the spectrum is. An outer gap can, in principle, generate pulse spectra extending up to tens of GeV (Zhang & Cheng 2000), while gaps close to surface high magnetic fields can produce steep spectra (photon index  $\lesssim 3$ ; Ramanamurthy et al. 1996) and cutoff in the tens of MeV range (PSR 1509–58, Harding et al. 1997). The absence of corresponding a gamma-ray pulse in phase with radio main peaks in Vela and PSR B1706–44 could then be ascribed to a gap-dependent spectral slope and not only to beam angle and viewing geometry differences.

The multiplicity and variety of features seen in *AGILE* light curves can pave the way to a parameterized standard model (e.g.,

with adjustable accelerating electric fields' strength and location in the magnetosphere) for pulsar gaps and their corresponding observed high-energy pulses. In this perspective, the *AGILE* light-curves' time resolution, currently limited only by the (continuously increasing) source count statistics, will eventually yield a pulsar gap map by coupling timing analysis and phase-resolved spectral analysis.

### 6.3. The Vela Glitch of 2007 August

During early *AGILE* observations, Vela experienced a weak glitch clearly detected in radio as a discontinuity in the pulsar's spin parameters.

Glitches are small ( $\Delta\nu/\nu \sim 10^{-9}$  to  $10^{-6}$ ) and sudden ( $\lesssim 1$  day) discontinuous increases in the pulsar frequency, often followed by a recovery (1–100 days) to the preglitch frequency. About  $\sim 6\%$  of pulsars are known to have shown glitches<sup>31</sup>, with a higher incidence of events in younger pulsars. This phenomenon is potentially a very promising tool for probing the physics of the neutron star interiors (Lyne et al. 2000). Although no general consensus has been reached to date about the origin of the glitches, many models are based on the exchange of angular momentum between the superfluid neutron star core and its normal, solid crust (Ruderman 1976, 1991; Alpar et al. 1984b, 1984a). This angular momentum transfer may excite starquake waves, propagating toward the neutron star surface. Since the magnetic field frozen in the crust is “shaken,” the resulting oscillating electromagnetic potential could generate strong electric fields parallel to the magnetic field, which in turn would accelerate particles to relativistic energies, possibly emitting a burst of high-energy radiation.

Since the first observation of a pulsar glitch in 1969 (Radhakrishnan & Manchester 1969), Vela has shown  $\sim 10$  major glitches. Due to its large FOV, the quest for possible gamma-ray bursting behavior due to a glitch is then an effective opportunity for *AGILE*. Despite the fact that the 2007 August glitch is a weak one ( $\Delta\nu/\nu \sim 10^{-9}$ ), it is worthwhile to search for a signal in the *AGILE* data.

The characteristic energy of a pulsar glitch can be roughly estimated from the associated pulsar frequency jump  $E_{\text{glitch}} = \Delta E_{\text{rot}} = 4\pi^2 I \nu \Delta\nu$ , where  $I$  ( $\sim 10^{45} \text{ g cm}^2$ ) is the neutron star momentum of inertia. The corresponding expected gamma-ray counts would be

$$C_{\gamma}^{\text{glitch}} = \eta \frac{E_{\text{glitch}} A_{\text{eff}}}{4\pi d^2 E_{\gamma}} \simeq 10^{11} \eta \frac{\Delta\nu}{\nu}, \quad (5)$$

where  $\eta = [0, 1]$  is the unknown conversion efficiency of the glitch energy to gamma-ray emission,  $d$  ( $\sim 0.3 \text{ kpc}$ ) is the pulsar distance,  $E_{\gamma}$  ( $\sim 300 \text{ MeV}$ ) is the average gamma-ray photon energy assuming a spectral photon index  $\Gamma = -2$ , and  $A_{\text{eff}}$  is the *AGILE* effective area.

Even in the virtual limit assumption that the entire glitch energy could be driven into gamma-ray emission, a weak glitch with a frequency shift of  $\Delta\nu/\nu = 1.3 \times 10^{-9}$ , as that observed in 2007 August, cannot produce a strong signal ( $C_{\gamma}^{\text{glitch}} < 100$ –200 counts), if the core fluence is spread in  $\sim 1$  day. In fact, no excess on daily timescales was detected, although for much shorter timescales of 3–6 min, a  $> 5\sigma$  excess ( $\sim 15$  counts) in the photon counts is seen at  $\sim 54,312.693 \text{ MJD}$  (Figure 9).

On the other hand, stronger Vela glitches, as that of 1988 Christmas (McCulloch et al. 1990) with a frequency shift of

<sup>31</sup> See, e.g., <http://www.atnf.csiro.au/research/pulsar/psrcat/>.

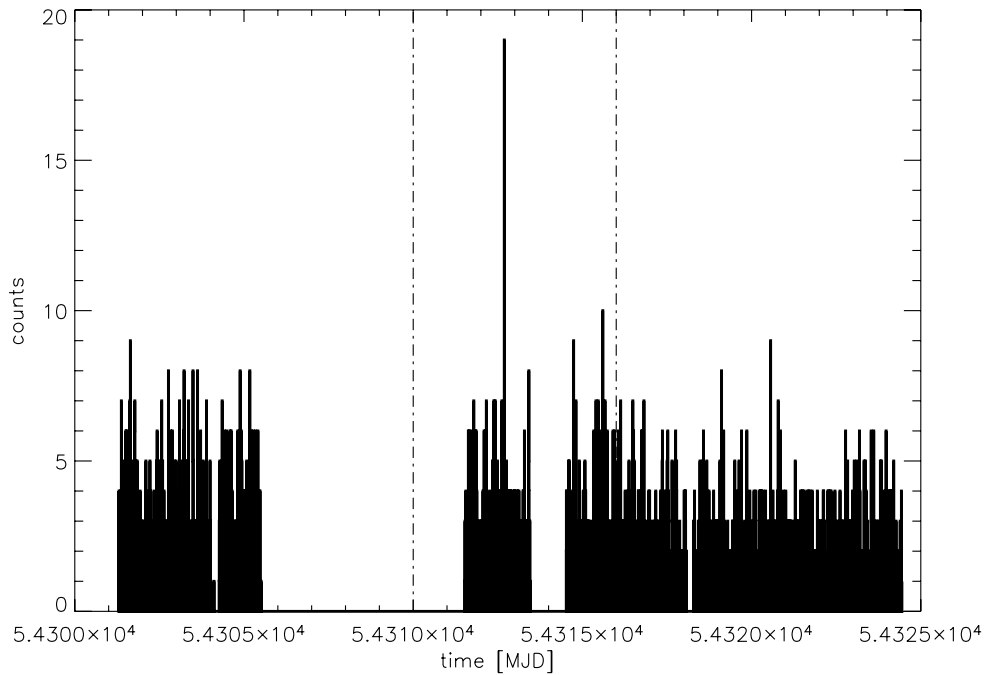


**Figure 9.** Unfolded Vela pulsar light curve (4.5 minute bin size,  $E > 50$  MeV, G-class events). Dashed lines bracket glitch epoch uncertainty range ( $54,313 \pm 3$  MJD).  $A > 5\sigma$  count excess at  $\sim 54,312.693$  MJD could be associated with gamma-ray bursting emission from the glitch.

$\Delta\nu/\nu = 2 \times 10^{-6}$ , could in principle produce more significant transient gamma-ray emission. The typical count rate from Vela is  $\sim 100$ – $200$  counts  $\text{day}^{-1}$ ; then, a fluence of  $\gtrsim 1000$  counts in  $\sim 1$  day or less from the hypothetical gamma-ray glitch burst should be easily detectable. According to Equation (5), such a flux could arise from a glitch with  $\Delta\nu/\nu \sim 10^{-7}$  (typical Vela glitch size), converting a relatively small fraction ( $\eta \sim 0.1$ ) of its energy in gamma rays. The chance occurrence of a strong Vela glitch in the *AGILE* FOV over 3 years of mission operations is of  $\sim 20\%$ .

## 7. CONCLUSIONS

*AGILE* collected  $\sim 15,000$  pulsed counts from known gamma-ray pulsars during its first nine months of operations. The *AGILE* PDHU clock stability, coupled with the exploitation of pulsar timing noise information, allows for pulsar period fitting with discrepancies with respect to radio measurements at the level of the period search resolution ( $\sim 10^{-12}$  s) over the long gamma-ray data span (greater than six months). Thanks to *AGILE* GPS-based high time tagging accuracy ( $\sim 1 \mu\text{s}$ ), the effective time resolution of *AGILE* light curves is limited only by the count statistics at the current level of exposure ( $\sim 1.2 \times 10^9 \text{ cm}^2 \text{ s}$  for the Vela region). The best effective time resolution obtained for Vela observations is of  $\sim 200 \mu\text{s}$  for a signal-to-noise  $> 3\sigma$  in the on-pulse light-curve bins. An improved effective time resolution of  $\lesssim 50 \mu\text{s}$  is expected after 3 years of *AGILE* observations.

*AGILE* multiwavelength phasing of the four gamma-ray pulsars is consistent with the results obtained by *EGRET*, although the high-resolution *AGILE* light curves shows narrower and structured peaks and new interesting features. In particular, a third peak is possibly detected at a  $\sim 3.7\sigma$  level in the Crab light curve, and several interesting features seem present in the Vela light curves.

In any case, the highly structured light curves hint at a complex scenario for the sites of particle acceleration in the

pulsar magnetospheres, implying different electric gaps with physical properties probably mostly related to their height above the neutron star surface. Alternatively, slight spatial oscillations of the gap locations on timescales  $\lesssim 1$  day could be invoked to explain the multiple contiguous peaks seen in the light curves.

The foreseen balance of count statistics at the end of the AO 1 observing program will allow for phase-resolved spectral analysis of the light curves and, correspondingly, a spatial mapping of the magnetospheric gaps (their altitude above the neutron star surface being possibly related to the shape of their spectra).

We finally note that the timing calibration and tests presented in this paper pave a way to an effective search for new gamma-ray pulsars with *AGILE*. The negligible discrepancies among the radio and the gamma-ray pulsar spin parameters seen in the known gamma-ray pulsars imply that the direct folding of the *AGILE* data on new pulsar candidates is a safe and efficient procedure, when the folding parameters are obtained from radio/X-rays ephemeris having a suitable epoch range of validity. In fact, gamma-ray period search trials around radio/X-rays solutions will be unnecessary when simultaneous ephemeris are available, strongly improving the detection significance for faint sources. According to the predicted gamma-ray pulsar luminosities ( $L_\gamma \propto \dot{E}^{1/2}/d^2$ ; e.g., Pellizzoni et al. 2004), the detection with *AGILE* of top-ranked Vela-like pulsars is then expected as soon as exposure levels  $\gtrsim 10^9 \text{ cm}^2 \text{ s}$  ( $E > 100$  MeV) will be attained for clean G-class events.

We acknowledge D. A. Smith, D. J. Thompson, and G. Tosti of GLAST Team for useful discussions on multiwavelength observations of pulsars and for their comments on the paper draft. J.P.H. was supported by NASA *XMM-Newton* grants NNX06AH58G and NNX07AU65G. A.P. and M.B. received financial support from the Italian Minister of Research (MIUR) under national program PRIN-MIUR 2005. The Parkes radio telescope is part of the Australia Telescope, which is funded

by the Commonwealth of Australia for operation as a National Facility managed by CSIRO. *XMM-Newton* is an ESA science mission with instruments and contributions directly funded by ESA Member States and NASA.

## REFERENCES

- Alpar, M. A., Anderson, P. W., Pines, D., & Shaham, J. 1984a, *ApJ*, **278**, 791
- Alpar, M. A., Pines, D., Anderson, P. W., & Shaham, J. 1984b, *ApJ*, 276, 325
- Argan, A. M., et al. 2004, in *IEEE Nuclear Science Symp.*, 1, 371
- Barbiellini, G., Bordignon, G., Fedel, G., Liello, F., Longo, F., Pontoni, C., Prest, M., & Vallazza, E. 2001, in AIP Conf. Ser. 587, Gamma 2001: Gamma-Ray Astrophysics, ed. S. Ritz, N. Gehrels, & C. R. Shrader (Melville, NY: AIP), 774
- Becker, W., & Pavlov, G. G. 2002, in *The Century of Space Science, Vol I*, ed. J. A. Bleeker, J. Geiss, & M. C. Huber (Dordrecht: Springer), 721
- Casandjian, J.-M., & Grenier, I. A. 2008, *A&A*, **489**, 849
- Cheng, K. S., Ho, C., & Ruderman, M. 1986, *ApJ*, **300**, 500
- Costa, E. L., et al. 2001, in AIP Conf. Ser. 599, X-ray Astronomy: Stellar Endpoints, AGN, and the Diffuse X-ray Background, ed. N. E. White, G. Malaguti, & G. G. C. Palumbo (Melville, NY: AIP), 582
- Daugherty, J. K., & Harding, A. K. 1996, *ApJ*, **458**, 278
- Dyks, J., Harding, A. K., & Rudak, B. 2004, *ApJ*, **606**, 1125
- Dyks, J., & Rudak, B. 2003, *ApJ*, **598**, 1201
- Edwards, R. T., Hobbs, G. B., & Manchester, R. N. 2006, *MNRAS*, **372**, 1549
- Fasano, G., & Franceschini, A. 1987, *MNRAS*, **225**, 155
- Feroci, M. E., et al. 2007, *Nucl. Instrum. Methods Phys. Res.*, **A581**, 728
- Fierro, J. M., Michelson, P. F., Nolan, P. L., & Thompson, D. J. 1998, *ApJ*, **494**, 734
- Harding, A. K., Baring, M. G., & Gonthier, P. L. 1997, *ApJ*, 476, 246
- Harding, A. K., Grenier, I. A., & Gonthier, P. L. 2007, *Ap&SS*, **309**, 221
- Harding, A. K., Stern, J. V., Dyks, J., & Frackowiak, M. 2008, *ApJ*, 680, 1378
- Harding, A. K., Strickman, M. S., Gwinn, C., Dodson, R., Moffet, D., & McCulloch, P. 2002, *ApJ*, **576**, 376
- Hartman, R. C. D. L., et al. 1999, *ApJS*, **123**, 79
- Hirota, K., & Shibata, S. 2001, *MNRAS*, **325**, 1228
- Hobbs, G., Lyne, A. G., Kramer, M., Martin, C. E., & Jordan, C. 2004, *MNRAS*, **353**, 1311
- Hobbs, G. B., Edwards, R. T., & Manchester, R. N. 2006, *MNRAS*, **369**, 655
- Jackson, M. S., & Halpern, J. P. 2005, *ApJ*, **633**, 1114
- Jansen, F. D., et al. 2001, *A&A*, **365**, L1
- Johnston, S., Lyne, A. G., Manchester, R. N., Kniffen, D. A., D'Amico, N., Lim, J., & Ashworth, M. 1992, *MNRAS*, **255**, 401
- Johnston, S., Manchester, R. N., Lyne, A. G., Kaspi, V. M., & D'Amico, N. 1995, *A&A*, **293**, 795
- Kanbach, G. 1990, in *The Energetic Gamma-Ray Experiment Telescope (EGRET) Science Symp.*, ed. C. E. Fichtel, S. D. Hunter, P. Sreekumar, & F. W. Stecker (Washington, DC: GPO), 101
- Kanbach, G. Z., et al. 1994, *A&A*, **289**, 855
- Kaspi, V. M., Lackey, J. R., Mattox, J., Manchester, R. N., Bailes, M., & Pace, R. 2000, *ApJ*, **528**, 445
- Kirsch, M. G. F., et al. 2004, in *Proc. SPIE 5165, X-Ray and Gamma-Ray Instrumentation for Astronomy XIII*, ed. K. A. Flanagan & O. H. W. Siegmund (Bellingham, WA: SPIE), 85
- Kramer, M. J. F., et al. 2003, *MNRAS*, **342**, 1299
- Kuiper, L., Hermsen, W., Verbunt, F., Ord, S., Stairs, I., & Lyne, A. 2002, *ApJ*, **577**, 917
- Kuiper, L., Hermsen, W., Verbunt, F., Thompson, D. J., Stairs, I. H., Lyne, A. G., Strickman, M. S., & Cusumano, G. 2000, *A&A*, **359**, 615
- Labanti, C. M., et al. 2006, in *Proc. SPIE 6266, Space Telescopes and Instrumentation. II. Ultraviolet to Gamma Ray*, ed. M. J. L. Turner & G. Hasinger (Bellingham, WA: SPIE), 62663Q
- Lyne, A. G., Pritchard, R. S., & Graham-Smith, F. 1993, *MNRAS*, **265**, 1003
- Lyne, A. G., Shemar, S. L., & Smith, F. G. 2000, *MNRAS*, **315**, 534
- Manchester, R. N., Hobbs, G. B., Teoh, A., & Hobbs, M. 2005, *AJ*, **129**, 1993
- Manchester, R. N. A. G., et al. 2001, *MNRAS*, **328**, 17
- Manzali, A., De Luca, A., & Caraveo, P. A. 2007, *ApJ*, **669**, 570
- McCulloch, P. M., Hamilton, P. A., McConnell, D., & King, E. A. 1990, *Nature*, **346**, 822
- Moffett, D. A., & Hankins, T. H. 1996, *ApJ*, **468**, 779
- Moffett, D. A., & Hankins, T. H. 1999, *ApJ*, 522, 1046
- Muslimov, A. G., & Harding, A. K. 2003, *ApJ*, **588**, 430
- Muslimov, A. G., & Harding, A. K. 2004, *ApJ*, **606**, 1143
- Peacock, J. A. 1983, *MNRAS*, **202**, 615
- Pellizzoni, A., Chen, A., Conti, M., Giuliani, A., Mereghetti, S., Tavani, M., & Vercellone, S. 2004, *Adv. Space Res.*, **33**, 625
- Perotti, F., Fiorini, M., Incorvaia, S., Mattaini, E., & Sant'Ambrogio, E. 2006, *Nucl. Instrum. Methods Phys. Res.*, **A556**, 228
- Pétri, J., & Kirk, J. G. 2005, *ApJ*, 627, L37
- Prest, M., Barbiellini, G., Bordignon, G., Fedel, G., Liello, F., Longo, F., Pontoni, C., & Vallazza, E. 2003, *Nucl. Instrum. Methods Phys. Res.*, **A501**, 280
- Radhakrishnan, V., et al. 1995, *ApJ*, **450**, 791
- Ramanamurthy, P. V., Fichtel, C. E., Kniffen, D. A., Sreekumar, P., & Thompson, D. J. 1996, *ApJ*, **458**, 755
- Romani, R. W. 1996, *ApJ*, **470**, 469
- Romani, R. W., & Yadigaroglu, I.-A. 1995, *ApJ*, **438**, 314
- Ruderman, M. 1976, *ApJ*, **203**, 213
- Ruderman, M. 1991, *ApJ*, **366**, 261
- Takata, J., & Chang, H.-K. 2007, *ApJ*, **670**, 677
- Tavani, M., et al. 2009, *A&A*, in press
- Tavani, M. G., et al. 2006, in *Proc. SPIE 6266, Space Telescopes and Instrumentation. II. Ultraviolet to Gamma Ray*, ed. M. J. L. Turner & G. Hasinger (Bellingham, WA: SPIE), 626603
- Thompson, D. J. 2004, in *Astrophysics and Space Science Library 304, Cosmic Gamma-Ray Sources*, ed. K. S. Cheng & G. E. Romero (Dordrecht: Kluwer), 149
- Thompson, D. J. M., et al. 1996, *ApJ*, **465**, 385
- Tompkins, W. F., Jones, B. B., Nolan, P. L., Kanbach, G., Ramanamurthy, P. V., & Thompson, D. J. 1997, *ApJ*, **487**, 385
- Yadigaroglu, I.-A., & Romani, R. W. 1995, *ApJ*, **449**, 211
- Zhang, L., & Cheng, K. S. 2000, *A&A*, **363**, 575